

A Spin-Optical Quantum Computing Architecture

Grégoire de Gliniasty,^{1,2,*} Paul Hilaire,^{1,*} Pierre-Emmanuel Emeriau,¹
Stephen C. Wein,¹ Alexia Salavrakos,¹ and Shane Mansfield¹

¹*Quandela, 7 Rue Léonard de Vinci, 91300 Massy, France*

²*Sorbonne Université, CNRS, LIP6, F-75005 Paris, France*

We introduce an adaptable and modular hybrid architecture designed for fault-tolerant quantum computing. It combines quantum emitters and linear-optical entangling gates to leverage the strength of both matter-based and photonic-based approaches. A key feature of the architecture is its practicality, grounded in the utilisation of experimentally proven optical components. Our framework enables the execution of any quantum error correcting code, but in particular maintains scalability for low-density parity check codes by exploiting built-in non-local connectivity through distant optical links. To gauge its efficiency, we evaluated the architecture using a physically motivated error model. It exhibits loss tolerance comparable to existing all-photonic architecture but without the need for intricate linear-optical resource-state-generation modules that conventionally rely on resource-intensive multiplexing. The versatility of the architecture also offers uncharted avenues for further advancing performance standards.

I. INTRODUCTION

Fault-tolerant (FT) quantum computing (QC) allows arbitrary quantum algorithms to be performed even in the presence of moderated yet non-negligible noise, thanks to the threshold theorem [1–3]. However appealing this concept might be in theory, the practical realization of a FT quantum computer is a highly nontrivial challenge.

A QC architecture is the association of two main ingredients. The first is a theoretical model for quantum computing such as gate-based [4], measurement-based [5], ancilla-driven [6] or adiabatic [7] quantum computing. The second is the organization of the hardware components that enables the physical implementation of this quantum computing model. Most proposals [8–14] for the physical implementation of FTQC rely on a modular approach. The concept of a *scalable* modular FT quantum computer revolves around a fundamental principle: while various module types may exist, the number of module categories, their specifications, and their quality should remain constant as the quantum computer grows in size. To ensure scalability, it is thus essential that the noise level of each hardware module remains independent of the quantum computer’s size, thereby preventing it from straying out of the fault-tolerant regime.

While it may seem self-evident, it is essential to underscore that a FTQC architecture designed for superconducting qubits will inherently differ from one tailored to linear optical systems which for instance lacks deterministic two-qubit gates. Crucially, an efficient FTQC architecture cannot be universally “hardware-agnostic”. It demands thorough adaptation to the unique characteristics of a particular platform and its corresponding noise model.

In the realm of photonic implementation, Ref. [14] proposed a modular photonic FTQC architecture, which places specific emphasis on the utilization of spontaneous parametric down-conversion (SPDC) sources in combination with linear-optical interferometers and detectors. However, these sources operate through a heralded generation process characterized by low probability, and entanglement is generated probabilistically using linear-optical gates.

On the other hand, in recent years we have witnessed the emergence of highly efficient single-photon sources, driven by a fundamentally distinct technology paradigm, specifically, the utilization of individual atoms or artificial atoms. Although SPDC sources had previously held the record for creating the largest photonic entangled states, atom-based single-photon sources have since surpassed them by generating a 14-qubit GHZ state [15]. These sources exploit the intricate interplay of light and matter, where the spin of the quantum emitter is coupled to the polarization of the emitted photon. Precise control over this spin enables the growth of photonic graph states. Contrary to SPDC sources, the quantum emitter’s spin mediates the generation of entanglement between photons which becomes a deterministic process. Moreover, single-photon sources based on trapped ions [16] or artificial atoms such as semiconductor quantum dots can exploit the same strategy to efficiently generate photonic graph states. The latter have already allowed experimental demonstration of photonic graph state generation [17–20], which it can achieve at rates that are orders of magnitude higher than atomic sources provided the photon collection efficiency is increased.

While quantum-emitter-based sources can replace SPDC sources to implement the architecture of Ref. [14] with a smaller footprint [21], it remains uncertain whether that scheme is optimally suited for these particular platforms. Indeed, these sources use a spin degree of freedom as a “photon entangler” to produce photonic entangled states [22, 23], which are potentially useful for

* These two authors contributed equally to this work

a fully-photonic QC. Yet, relying solely on the quantum emitter as a source of entangled photons might not be the optimal strategy either, as there is potential to harness its spin qubit to encode and process quantum information, thus maximizing its utility. What we need is a hybrid architecture combining the best of both worlds, by exploiting both the spin and photonic qubits to their full potential.

In this paper, we introduce a modular and scalable FTQC architecture tailored for quantum-emitter-based platforms. Our study delves into the investigation of its performance characteristics with a precise characterisation of the thresholds for quantum error correction in the presence of a realistic noise model. In this framework, the physical qubits are encoded in the quantum emitters, while the photons are used as ancilla qubits. We use these ancilla photons to implement nearly-deterministic gates between different emitters, employing a repeat-until-success (RUS) linear-optical scheme [24]. We also investigate a variant called hybrid RUS gates to boost the tolerance with respect to coherence time of the spin at the expense of loss tolerance.

The paper is organized as follows. In Sec. II, we detail the hardware layout of our quantum computing architecture. In Sec. III, we focus on the linear-optical RUS gate on which our architecture heavily relies to generate two-qubit entanglement. We compare our architecture to others in Sec. V. We then present in Sec. IV the performance in terms of FT thresholds of our architecture, based on a physically relevant error model. We finally discuss our results, compare them with the literature in Sec. V, and conclude in Sec. VI.

II. SPIN-OPTICAL QUANTUM COMPUTING ARCHITECTURE

In the following, we present our proposal for a FTQC architecture, hereafter referred to as the spin-optical quantum computing (SPOQC) architecture. This approach adopts a modular design specifically tailored for quantum emitter platforms. In this architecture, each quantum emitter is assumed to embed a qubit degree of freedom – its spin – and is capable of emitting spin-entangled photonic qubits. Crucially, we do not require direct interaction between quantum emitters, which makes this approach also suitable even for isolated quantum emitters. Instead, we use photons to mediate the two-qubit gates between the spins of non-interacting quantum emitters. This is achieved through linear-optical gates, in particular RUS gates, which will be discussed in greater detail later in this paper.

A. Global overview of the architecture

We first provide a global overview of the SPOQC architecture, illustrated by Fig. 1. Importantly, this archi-

tecture is compatible with any quantum error correcting (QEC) code. In particular, it is *scalable* for quantum low-density parity check (LDPC) codes [3, 26, 27] and can implement codes with *non-local connectivity*. This important category of codes encompasses many well-known QEC codes, including the well-established surface codes [3] but also the recently discovered “good” LDPC codes [28, 29], i.e. LDPC codes with constant encoding rate and linear distance.

To enable the fault-tolerance capabilities of a QEC code, efficient error detection is essential, requiring the use of dedicated “check” qubits. In the SPOQC architecture, each data or check qubit corresponds to a spin qubit within a quantum emitter, and their arrangement mirrors the connectivity defined by the QEC code’s Tanner graph. This graph serves as a useful visual representation of the QEC code’s structure. In this graph, each edge corresponds to optical links, such as fibers, a linear-optical interferometer, and photon detectors. This setup enables the execution of linear-optical gates between photons from different quantum emitters, ultimately resulting in the implementation of a two-qubit spin entangling gate. Crucially, if a spin node in the graph has more than one neighbor (which is usually the case), it requires an optical router to orient the photons to the correct photonic link.

For quantum LDPC codes [30], each node of the Tanner graph has a bounded number of neighbors which is critical for the scalability of the architecture. Without this constraint, the number of output modes of some photon routers could potentially become unbounded as the size of QEC code increases. The architecture remains inherently fault-tolerant as long as the FT gates require a bounded amount of additional connectivity between the physical qubits. This is for example the case for surface code implementations with lattice surgery and magic state distillation [31].

Fig. 1 summarizes the essential features of the SPOQC architecture, taking the 3×3 rotated surface code as an example. We use the Tanner graph of the QEC code (Fig. 1(a)) to design the macroscopic physical layout of the architecture (Fig. 1(b)), based on simple optical modules. The connectivity of this layout enables the indirect measurement of stabilizers using check qubits. Physically, each qubit is encoded in a quantum emitter’s spin and the entangling gates are implemented optically using the linear-optical interferometer depicted in Fig. 1(c). In the following we present this architecture in more detail.

B. Tanner graph of a quantum error correcting code

A FT quantum computer relies on quantum error correction to actively detect and correct errors. Quantum logic gates can be implemented fault-tolerantly using different strategies depending on the QEC code being used, such as magic state distillation [32], lattice surgery [33],

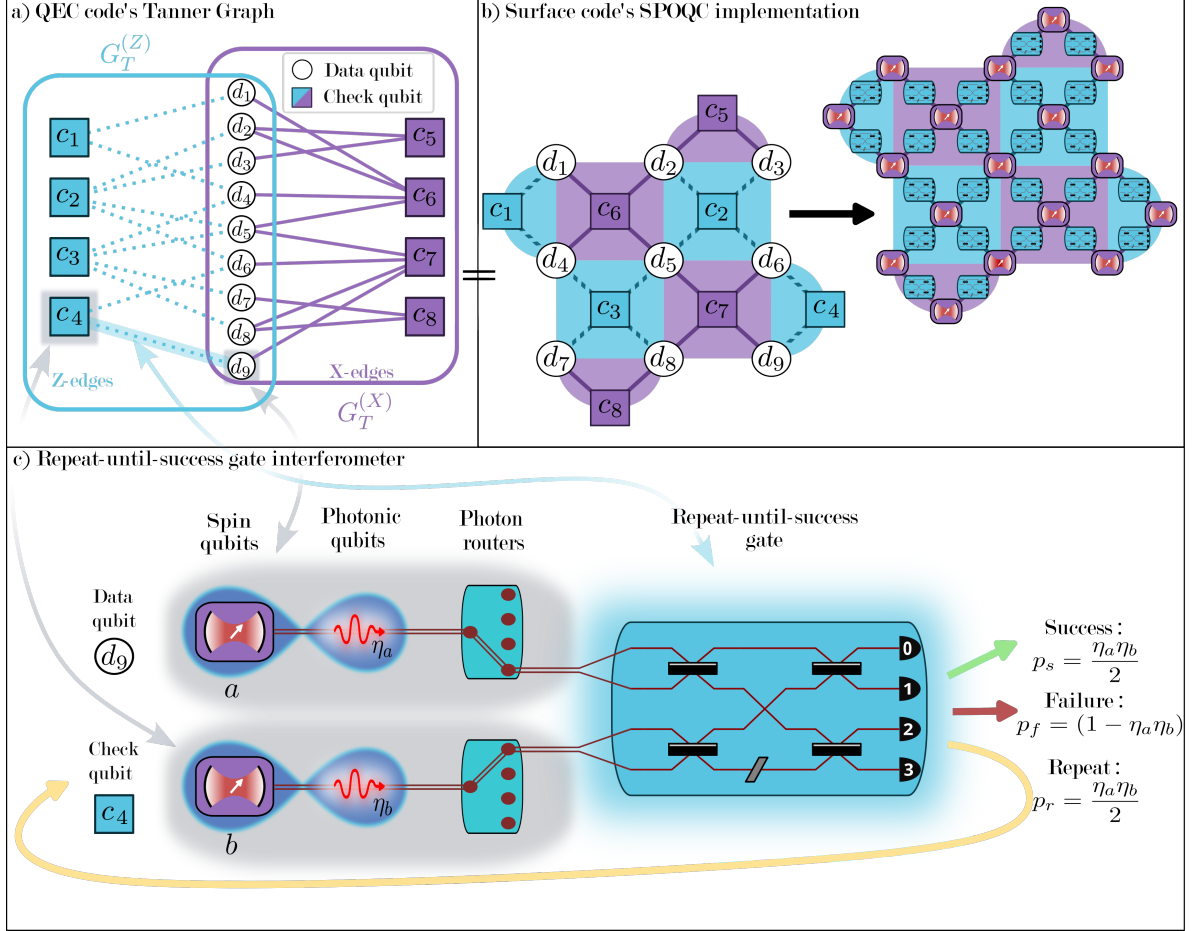


Figure 1. (a) Tanner graph of a 3×3 rotated surface code with its subgraphs $G_T^{(X)}$ and $G_T^{(Z)}$. X -edges (solid, violet) and Z -edges (dashed, blue) belong respectively to $E_T^{(X)}$, and $E_T^{(Z)}$. (b) Macroscopic architecture for a rotated surface code. Left: The previous Tanner graph represented in a planar layout. Right: The SPOQC architecture for the 3×3 rotated surface code. (c) Linear-optical repeat-until-success gate including spin qubits capable of emitting entangled photons, coupled to photon routers, an interferometer and detectors. The linear-optical interferometer (produced using the *Perceval* [25] framework) performs the unitary from Eq. (1). Horizontal black rectangles correspond to 50 : 50 beamsplitters, the inclined parallelogram corresponds to a $-\pi/2$ phase shifter, numbered semiovals are photon-number-resolving detectors.

or code switching [34]. In the following, we will not consider the different methods to implement FT gates but instead orient our discussion to focus on the robustness of our quantum computing architecture to errors. In accordance with the threshold theorem [1–3], for a specific error model, any quantum algorithm can be executed fault-tolerantly, under the condition that the physical errors remain below a certain threshold value, and that the FT quantum computer is sufficiently large. This threshold value depends on the chosen methods for implementing error correction and the specific QEC code employed.

In an $[[n, k, d]]$ QEC code, n data qubits encode $k < n$ logical qubits to protect them from at least $t = \lfloor (d-1)/2 \rfloor$ qubit errors (or $d-1$ qubit losses). Errors are identified by measuring stabilizer check operators which depend on the QEC code being used.

In an $[[n, k, d]]$ stabilizer QEC code, there are $(n-k)$ independent stabilizer check operators, which are multi-qubit Pauli operators acting on the n data qubits. These specify the “inner structure” of the code that codewords (i.e. valid logical quantum states) should abide by: for any stabilizer check operator K in a given stabilizer QEC code, any codeword $|\psi\rangle_L$ should meet the condition $K|\psi\rangle_L = +1|\psi\rangle_L = (-1)^m|\psi\rangle_L$ with $m=0$. Therefore, measuring a stabilizer check operator should always give you an “ $m=0$ ” outcome and obtaining an “ $m=1$ ” outcome corresponds to an erroneous state. The bit string of all the stabilizer measurement outcomes is the error syndrome that a decoder uses to (ideally) identify the most likely error that occurred and correct it.

More general types of codes, such as the subsystem codes [35], the Floquet codes and the instantaneous stabilizer group codes [36, 37] operate differently but are

still based on the measurements of stabilizer check operators. The central QEC properties originate from these stabilizer measurements and being able to decode them (efficiently) to identify errors. Throughout this paper, we will use the $d \times d$ rotated surface code [38], which is a $[[d^2, 1, d]]$ QEC code, as an illustrative example for our architecture.

The Tanner graph of a QEC code is a bipartite graph $G_T = (V_T, E_T)$, with $V_T = V_T^{(d)} \sqcup V_T^{(c)}$, with properties we will now describe. Vertices in $V_T^{(d)}$ correspond to physical *data* qubits, while vertices in $V_T^{(c)}$, denoted check vertices, correspond to stabilizer check operators (which can be later associated to physical *check* qubits). The edge set can be decomposed in three disjoint sets $E_T = E_T^{(X)} \sqcup E_T^{(Y)} \sqcup E_T^{(Z)}$. An undirected edge $(d_i, c_j) \in E_T^{(A)}$ (for $A \in \{X, Y, Z\}$) connects a check vertex $c_j \in V_T^{(c)}$ with a data vertex $d_i \in V_T^{(d)}$ in the Tanner graph whenever the associated stabilizer check operator acts non-trivially on the data qubit through the Pauli operator A on the QEC code. For example, if d_1, d_2, d_3 is the set of neighbors of a check vertex $c_j \in V_T^{(c)}$, with respective edges in $E_T^{(X)}, E_T^{(Y)}, E_T^{(Z)}$, then the associated stabilizer check is $K_{c_j} = X_{d_1}Y_{d_2}Z_{d_3}$. Figure 1(a) represents the Tanner graph of the $d \times d$ rotated surface code [38].

A Calderbank-Shor-Steane (CSS) code has only X -type or Z -type stabilizer check operators; i.e. stabilizer check operators consist either entirely of X s and I s or of Z s and I s. Therefore, for any check vertex $c_j \in V_T^{(c)}$, its incident edge set $E_T(c_j) = \{(d_i, c_j) \in E_T\}$ is either included in $E_T^{(X)}$ or in $E_T^{(Z)}$ ($E_T^{(Y)} = \emptyset$). We can thus divide $V_T^{(c)}$ into two disjoint subsets $V_T^{(c,X)}$ and $V_T^{(c,Z)}$ for X -type and Z -type stabilizer check operators respectively. From G_T we can thus obtain two subgraphs, $G_T^{(X)} = (V_T^{(d)} \sqcup V_T^{(c,X)}, E_T^{(X)})$ and $G_T^{(Z)} = (V_T^{(d)} \sqcup V_T^{(c,Z)}, E_T^{(Z)})$, also known as (classical) Tanner graphs. In fact these graphs fully specify a CSS code and can also be used to design efficient decoders [39, 40]. The low-density parity check property of a family of code implies that the Tanner graph of each code from this family has a bounded degree, i.e. each vertex has a maximum number of neighbors. For example, the family of $d \times d$ rotated surface codes is not only CSS but also LDPC, since $\forall d \in \mathbb{N}, \forall v \in V_T, |E_T(v)| \leq 4$.

C. Stabilizer measurements with RUS gate

A crucial part of FTQC revolves around the accurate measurements of stabilizer check operators. They are usually challenging to measure directly since they involve multiple qubits. As a workaround, stabilizer measurements are often performed indirectly by leveraging check qubits. The quantum circuit for indirectly measuring a stabilizer check operator K with the assistance of a check

qubit “c” is illustrated in Fig. 2. In this figure, the CZ gate representation is unconventional as they are RUS CZ gates. For the time being, we can set aside this particular detail. This quantum circuit effectively projects onto the subspace stabilized by $(-1)^m K_c$, where $m \in \{0, 1\}$ is the measurement outcome of the check qubit. This outcome is subsequently used by the decoder to detect and correct errors in the quantum computation process.

In the context of the SPOQC architecture, deterministic CZ gates are unavailable, and we substitute them with RUS CZ gates. These gates are elaborated upon in Sec. III. Despite their inherent probabilistic nature, RUS CZ gates offer the advantage of being *heralded* gates. This means that we can ascertain whether a gate has succeeded, failed or been aborted, providing valuable information for the decoder. Consequently, a failed or aborted gate can be treated as a heralded error, which typically presents a more manageable decoding problem because the decoder can potentially harness not only the measurement outcome m but also the heralded outcomes of each RUS CZ gate m_i corresponding to the target data qubit involved in the RUS CZ gate with the qubit “c” (see Fig. 2).

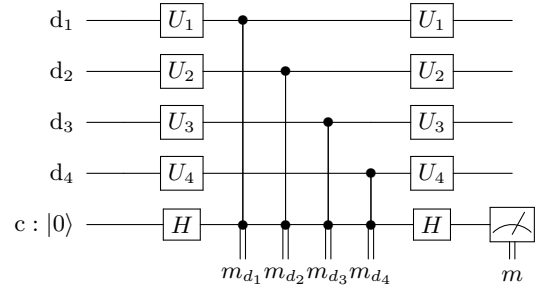


Figure 2. General quantum circuit for an indirect stabilizer measurement using a check qubit “c” (illustrated for a weight-4 stabilizer check operator). We measure $K_c = A_{d_1} \otimes A_{d_2} \otimes A_{d_3} \otimes A_{d_4}$ by using this circuit and by setting U_i to be $H = H_{XZ} = (X + Z)/\sqrt{2}$ when $A_{d_i} = X_{d_i}$, by setting it to $H_{YZ} = (Y + Z)/\sqrt{2}$ when $A_{d_i} = Y_{d_i}$, and by setting it to I_{d_i} when $A_{d_i} = Z_{d_i}$. If the measurement outcome is $m = 0$ (respectively $m = 1$), the system is projected onto the subspace stabilized by K_c (resp. $-K_c$). In this circuit, each conventional CZ gate is replaced by a RUS CZ gate. To indicate a RUS CZ, we decorate a usual CZ with a classical wire that indicates the heralding outcome m_{d_i} which can either herald a success, a failure or an abort signal.

D. Modules of the physical architecture

In the following, we present the physical layout of the SPOQC architecture, which is designed with a modular structure. We provide a description of each of its primary modules.

a. Quantum emitter module. A quantum emitter module includes a quantum emitter with a spin qubit,

and all its control components for single-photon emission and spin control. We will assume that we have full $SU(2)$ control on the spin qubit and that it can emit spin-entangled photons through the emission gate $E_{\text{qe,ph}} = |0_{\text{qe}}, 0_{\text{ph}}\rangle\langle 0_{\text{qe}}| + |1_{\text{qe}}, 1_{\text{ph}}\rangle\langle 1_{\text{qe}}|$, or equivalent [15, 18–20, 41]. The quantum emitter sends photons in a privileged single direction, optimising the efficient collection of photonic qubits (for example using a fiber) [15, 42–45]. The control components within the system are operated through classical information processing. For instance, we rely on classical information to determine whether to proceed with emitting a new spin-entangled photon and initiating a new trial. This decision is contingent upon receiving information that heralds either the success, partial failure, or complete failure of a RUS gate trial.

b. Quantum channel. The propagating photons are transferred from one module to another thanks to quantum channels that can be implemented using optical fibers or free-space components.

c. Photon router module. The photon router module is an active component that routes photons from a specified input to a designated output [46–48]. In our modules, we employ a $1 \times N$ router configuration, where photons originating from a single mode can be routed to any of the N output modes. The routing strategy depends on information transmitted to the router via a classical channel.

d. RUS gate module. A RUS gate module takes as input two photonic qubits and performs a linear-optical transformation followed by photon detection. It sends the detector measurement outcome through classical channels.

E. Macroscopic layout of the physical architecture

In the following, we explore how we can exploit the fault-tolerant properties of a given QEC code using an arrangement of the preceding modules.

Based on the QEC Tanner graph and the previously introduced modules, we propose the following layout. The data and check qubits of a QEC code are encoded using the spin qubits of quantum emitters. Therefore, for each data or check qubit, corresponding to a vertex in the Tanner graph, we use a single quantum emitter module. Each quantum emitter module is connected to a photon router module thanks to a quantum channel (e.g. a fiber).

The SPOQC architecture is ideal for LDPC codes because the largest number of photon router outputs necessary to perform every stabilizer measurement circuits corresponds to the Tanner graph’s maximum degree. Yet, increasing the number of outputs of each photon router could also offer other advantages such as enabling fault-tolerant gates [49], single-shot error correction [50], or increasing the compilation speed [51].

If there is an edge between vertices $c_j \in V_T^{(c)}$ and $d_i \in V_T^{(d)}$, a RUS gate module should be connected to one of

the output ports of the photon router modules of both the corresponding check qubit c_j and data qubit d_i . Note that the edge type, X, Y, Z , can be decided by applying a Hadamard gate $H = H_{XZ} = (X+Z)/\sqrt{2}$, a Y-Hadamard gate $H_{YZ} = (Y+Z)/\sqrt{2}$ or the identity gate on qubit d_i just before and immediately after the RUS CZ gate as shown in Fig. 2.

The example given in Fig. 1(b) shows this architecture implemented for a local code – the 3×3 rotated surface code whose Tanner graph was previously introduced in Fig. 1(a). Note, however, that contrary to other architectures, the SPOQC architecture uses long-range optical links and is thus not restricted to codes respecting locality constraints. This allows it to implement any QEC code, and in particular it is scalable for any LDPC code.

III. REPEAT-UNTIL-SUCCESS LINEAR-OPTICAL GATES

A. General overview

In this section, we focus on the repeat-until-success (RUS) gates which are central to this architecture. In its broadest sense [52, 53], a RUS implementation of a quantum gate U relies on the repetition of a non-deterministic quantum circuit C involving measurements. C should be repeated until one of the measurement outcomes corresponding to the successful implementation of U is obtained. Critically, the other measurement outcomes should, up to some local correction, correspond to the identity gate so that it can be repeated indefinitely.

Here, however, following the original terminology [24], the term RUS gate will refer specifically to the CZ gate, whose non-deterministic circuit is realised by the emission of entangled photons passing through a linear optical circuit before being detected.

Note that linear-optical RUS gates typically have higher success rates for a given amount of loss than ancilla-assisted fusion gates and boosted fusion gates [21] when compared to other common linear-optical gates used for generating entanglement. This is why we can expect an improved loss tolerance compared to other implementations without sacrificing the architecture’s simplicity. RUS gates have been proposed to generate graph states [54], including the “Raussendorf-Harrington-Goyal” lattice [55, 56], where the qubits in the graph states are the quantum-emitter qubits. A recent protocol [57] uses a linear-optical RUS gate to generate a $|W\rangle$ entangled state on d quantum emitters which can then be used to generate photonic qudit GHZ states near-deterministically.

Below, we provide an in-depth presentation of these RUS gates.

B. Quantum emitter

In addition, we consider quantum emitters that have a degree of freedom, such as a spin on which we can encode a qubit, $|0\rangle_{\text{qe}} = |\uparrow\rangle_{\text{qe}}$, $|1\rangle_{\text{qe}} = |\downarrow\rangle_{\text{qe}}$. Hereafter, note that while we informally refer to this degree of freedom as a “spin”, it can represent any pair of energy-level states within the quantum emitter. We also consider that one of the single-photon degrees of freedom, such as its polarization or its path, encodes a qubit. This degree of freedom can also be entangled with the spin state upon emission, with an emission process described by the operator

$$E_{\text{qe,ph}} = |0\rangle_{\text{qe}} |0\rangle_{\text{ph}} \langle 0|_{\text{qe}} + |1\rangle_{\text{qe}} |1\rangle_{\text{ph}} \langle 1|_{\text{qe}}.$$

This operator permits the emission of spin-entangled photons [23]. For example, if the spin is initialized to $|+\rangle_{\text{qe}} = |0\rangle_{\text{qe}} + |1\rangle_{\text{qe}}$ (omitting state normalisation), after the emission of a photon, the resulting state is $E_{\text{qe,ph}} |+\rangle_{\text{qe}} = |0\rangle_{\text{qe}} |0\rangle_{\text{ph}} + |1\rangle_{\text{qe}} |1\rangle_{\text{ph}}$.

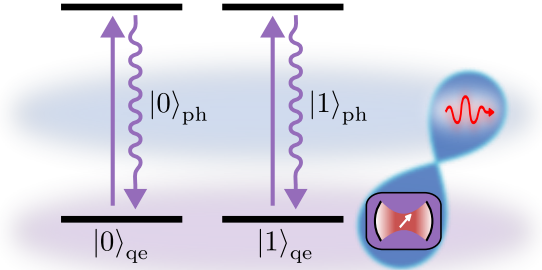


Figure 3. Quantum emitter level structure. The optical transitions, represented in violet, enable the emission of a spin-entangled photon following operator $E_{\text{qe,ph}}$.

A quantum emitter that naturally allows the emission of spin-entangled photons through the operator $E_{\text{qe,ph}}$ is a singly-charged quantum dot whose energy levels form a four-energy-level system with two optical transitions as shown in Fig. 3 [17–19]. In this system, the photonic qubits are encoded using the polarization degree of freedom. However, this emission process is by no means restricted only to such a level structure and can be adapted to many other configurations and most quantum emitter platforms, such as other types of quantum dots, atoms, superconducting circuits, and color defects [15, 41, 58–63].

C. Photonic qubits

The quantum emitter described in Fig. 3 emits photons entangled in polarization but it is straightforward to convert polarization-encoded photonic qubits into path-encoded photonic qubits, for example using a polarizing beamsplitter. In path encoding, $|0\rangle_{\text{ph}} = |1, 0\rangle_{\text{ph}}$,

$|1\rangle_{\text{ph}} = |0, 1\rangle_{\text{ph}}$, where $|i, j\rangle$ corresponds to having i (j) photons in the first (second) spatial mode. We will use the path encoding for the linear-optical interferometer description in the following.

D. Linear-optical interferometer

The linear-optical interferometer presented in Fig. 1(c) implements the following unitary transformation on the photonic modes (a variant of that found in Ref. [24])

$$U = \frac{1}{2} \begin{pmatrix} 1 & 1 & 1 & 1 \\ 1 & 1 & -1 & -1 \\ 1 & -1 & -i & i \\ 1 & -1 & i & -i \end{pmatrix}. \quad (1)$$

which we use to perform a (CZ) RUS gate.

The input modes 0 and 1 (respectively 2, 3) correspond to the dual-rail modes of the photonic qubits emitted by quantum emitter a (respectively quantum emitter b). Four photon-number-resolving (PNR) detectors are positioned at the output modes of the interferometers. If PNR detectors are not available, it is also possible to build a pseudo PNR detector out of beamsplitters and many threshold detectors [64]. We denote by (k, l) a detection pattern where detectors in output modes k and l each detect a single photon. Note that (k, l) is also equivalent to the detection pattern (l, k) . A detection event (k, k) corresponds to the detector in output mode k detecting two photons.

A comprehensive description of the functioning of the RUS gate is provided in the following.

a. Emission step. In each trial, every quantum emitter sends an entangled photon through the operation $E_{\text{qe,ph}}$ into the linear-optical interferometer. The photons are detected at the output modes of the interferometers. The spin gate that has been performed depends on the detection pattern.

b. Successful measurement outcomes. Some measurement outcomes such as $(0, 2)$, i.e. a photon detected at output mode 0 and a photon detected at output mode 2, correspond to a spin CZ gate up to single-qubit unitary corrections, e.g. $S_a S_b^\dagger$ in the $(0, 2)$ case. Here, $S_i = \sqrt{Z_i}$ is the phase gate on qubit i . When performing these corrections, we obtain a successful spin CZ gate and the RUS gate has succeeded at this trial.

c. “Repeat” measurement outcomes. Other measurement outcomes such as $(2, 2)$, i.e. two photons detected at output mode 2, correspond to an identity gate up to correction, e.g. $Z_a Z_b$ for the $(2, 2)$ case. In that case, we have not performed the desired CZ gate but we can try again by re-emitting photons into the interferometer, until we obtain a successful measurement outcome.

d. Gate failure. A RUS gate fails at a given trial, denoted as an \mathcal{F} detection pattern, if strictly less than two photons are detected. Such an event can only happen in the presence of photon loss (including imperfect efficiency

Detection	(0, 2)	(1, 3)	(0, 3)	(1, 2)	(0, 0)	(1, 1)	(0, 1)	(2, 2)	(3, 3)	(2, 3)	\mathcal{F}
Probability	$\frac{\eta_a \eta_b}{8}$	$\frac{\eta_a \eta_b}{8}$	$\frac{\eta_a \eta_b}{8}$	$\frac{\eta_a \eta_b}{8}$	$\frac{\eta_a \eta_b}{8}$	$\frac{\eta_a \eta_b}{8}$	0	$\frac{\eta_a \eta_b}{8}$	$\frac{\eta_a \eta_b}{8}$	0	$1 - \eta_a \eta_b$
Corrections	$S_a S_b^\dagger$		$S_a^\dagger S_b$		Id			$Z_a Z_b$			Id
Spin Gate	$CZ_{a,b}$				Id						$C_{RUS,f}$

Table I. RUS gate detection patterns and associated transformations. The first row corresponds to the detection pattern that has been observed, noting that the last column \mathcal{F} corresponds to all cases for which one or both photons have been lost. The second row is the detection event probability (for mixed input state and indistinguishable photons). The third and fourth rows correspond to the spin corrections and the gates between spins that are performed.

of the detectors). In that case, we lose partial information of the spin states, and the corresponding channel corresponds to a spin phase erasure applied to the two quantum emitters,

$$C_{RUS,f} = C_{Z_a} C_{Z_b} = C_{Z_b} C_{Z_a}$$

where

$$C_{Z_i}(\rho) := \frac{1}{2}(\rho + Z_i \rho Z_i).$$

Indeed, it is easy to show that $C_{Z_i}(\rho) = \text{Tr}_{\text{ph}}(E_{i,\text{ph}} \rho E_{i,\text{ph}}^\dagger)$, i.e. emitting a photon from quantum emitter i and tracing this photon out to denote it being lost. If we lose both photons it is clear that we apply $C_{RUS,f}$. If we lose only one photon, the linear-optical interferometer erases the “which-path” information of the detected photon, so that we don’t know which quantum emitter produced it. Therefore, in that case as well, we should apply $C_{RUS,f}$.

Detection events along with their resulting correction unitaries and spin gates are summarized in Table I [65].

E. Success rate

From Table I, it is clear that each gate trial has a success rate of $p_s = \eta_a \eta_b / 2$, a “repeat” rate of $p_r = \eta_a \eta_b / 2$ and a failure probability of $p_f = 1 - \eta_a \eta_b$, where η_i is the end-to-end transmission efficiency (i.e. from photon emission to detection) of a photon emitted by quantum emitter i . Whenever a trial yields a repeat pattern, we can try again. Therefore the overall RUS gate success rate is given by:

$$\begin{aligned} P_{\text{RUS},s}(\eta_a, \eta_b, k) &= p_s \sum_{n=0}^{k-1} (p_r)^n \\ &= \frac{\eta_a \eta_b}{2} \frac{1 - (\eta_a \eta_b / 2)^k}{1 - \eta_a \eta_b / 2} \\ &\xrightarrow{k \rightarrow +\infty} \frac{\eta_a \eta_b}{2 - \eta_a \eta_b} \end{aligned} \quad (2)$$

where k is the maximum number of trials allowed, since in practice a gate cannot take infinite time. Similarly,

the failure rate is

$$\begin{aligned} P_{\text{RUS},f}(\eta_a, \eta_b, k) &= p_f \sum_{n=0}^{k-1} (p_r)^n \\ &= (1 - \eta_a \eta_b) \frac{1 - (\eta_a \eta_b / 2)^k}{1 - \eta_a \eta_b / 2} \\ &\xrightarrow{k \rightarrow +\infty} \frac{2 - 2\eta_a \eta_b}{2 - \eta_a \eta_b}, \end{aligned} \quad (3)$$

and the aborted rate (where no gate is applied) is

$$\begin{aligned} P_{\text{RUS},a}(\eta_a, \eta_b, k) &= 1 - [P_{\text{RUS},s} + P_{\text{RUS},f}](\eta_a, \eta_b, k) \\ &\xrightarrow{k \rightarrow +\infty} 0. \end{aligned} \quad (4)$$

Since we maximize the gate success probability by repeating it until it succeeds or fails, the RUS gates are quite efficient at performing a gate between remote qubits using linear-optics. However, between each trial step of the gate, we need a round of communication between the quantum emitter modules and the RUS module. Indeed, a pair of photons should be transferred from a quantum emitter towards the detectors and the classical information of the measurement outcome should be transferred back to the quantum emitter’s nodes to decide whether we should or not proceed with a next trial. Given a distance L_0 between the quantum emitter and the detectors, this implies a waiting time of at least $2L_0/c$, with c the speed of light, between two trials. Therefore, to avoid infinite gate time which are not feasible in practice, we should allocate a maximum number k of trials. In that case, if the gate is limited by the communication time delays, it lasts at least $2kL_0/c$.

IV. NUMERICAL RESULTS

In this section, we present the numerical results that we obtained with the SPOQC architecture. While this architecture can operate for any QEC stabilizer code, we consider rotated surface codes with a Minimum Weight Perfect Matching (MWPM) decoder to facilitate the comparison with other existing architectures. We use Stim [66] and Pymatching [67, 68] for our simulations.

We center our analysis on the error thresholds and we estimate them by calculating the crossing point of logical error curves for different code distances [69, 70].

Because we use distances up to 13, the values provided for thresholds are lower bounds on the actual thresholds. Our analysis centers on a physically-motivated error model that focuses on photonic errors and spin decoherence. In particular, we focus on the loss threshold and the spin decoherence time to reveal an interesting interplay between these two types of errors that arises from the physical implementation of an FT scheme with probabilistic RUS gates. We also consider partial distinguishability between the photons which causes errors in the RUS gates. To the best of our knowledge, this is the first time that an FT threshold has been derived for such an intrinsically photonic error. This model allows us to gain a comprehensive understanding of how these specific errors affect the performance of our architecture. Details about these error simulations can be found in Appendix B.

A. Independent RUS gate thresholds

a. RUS gate failure threshold. We first start by evaluating the threshold in terms of RUS gate failure or abort probability $p_F(\eta_a, \eta_b, k) = 1 - P_{\text{RUS},s}(\eta_a, \eta_b, k)$. Abort cases for RUS gates arise when the gate was neither a success nor a failure while the maximum number of allowed trials was exhausted resulting in an identity gate applied on the spins. For simplicity when running the simulations, we treat abort cases the same way as failure cases and apply the error $C_{\text{RUS},f}(\rho)$, which thus overestimates the amount of noise. Given that a realistic RUS gate depends on the maximum allowed number of trials k , this allows it to be evaluated simultaneously for all k . Assuming no spin decoherence $T_2 = +\infty$, and perfectly indistinguishable photons, we find the gate failure threshold $p_{F,\text{th},0} = 10.24 \pm 0.04\%$ in Fig. 4 (a) for an implementation of the SPOQC architecture with a rotated surface code. The interested reader can find details about our simulation methods in Appendix C. Assuming infinite decoherence time and uniform loss, we can in principle take as many trials as needed $k \rightarrow \infty$ and obtain a single-photon loss threshold approaching $1 - \eta_{\text{th}} = 2.75 \pm 0.02\%$.

b. Spin decoherence time. A spin qubit is usually described by two figures of merit, its relaxation time T_1 and its decoherence time T_2 . In the following, we consider that the spin decoherence is the main source of errors of our quantum emitters: $T_2 \ll T_1$, which is usually the case for quantum emitter platforms. We will not consider the spin relaxation time as a source of error ($T_1 = +\infty$) and only focus on the decoherence time T_2 . It is meaningful to express this decoherence time relative to the time required to perform a RUS gate t_{RUS} . We should thus obtain a threshold for the ratio t_{RUS}/T_2 : below a threshold value t_{th} , we are in the FT regime. Note that here again, we consider the time t_{RUS} for a full RUS gate so that we can evaluate it simultaneously for all k . We assume that one trial of the RUS gate takes a time t_{trial} , such that $t_{\text{RUS}} = kt_{\text{trial}}$. As shown

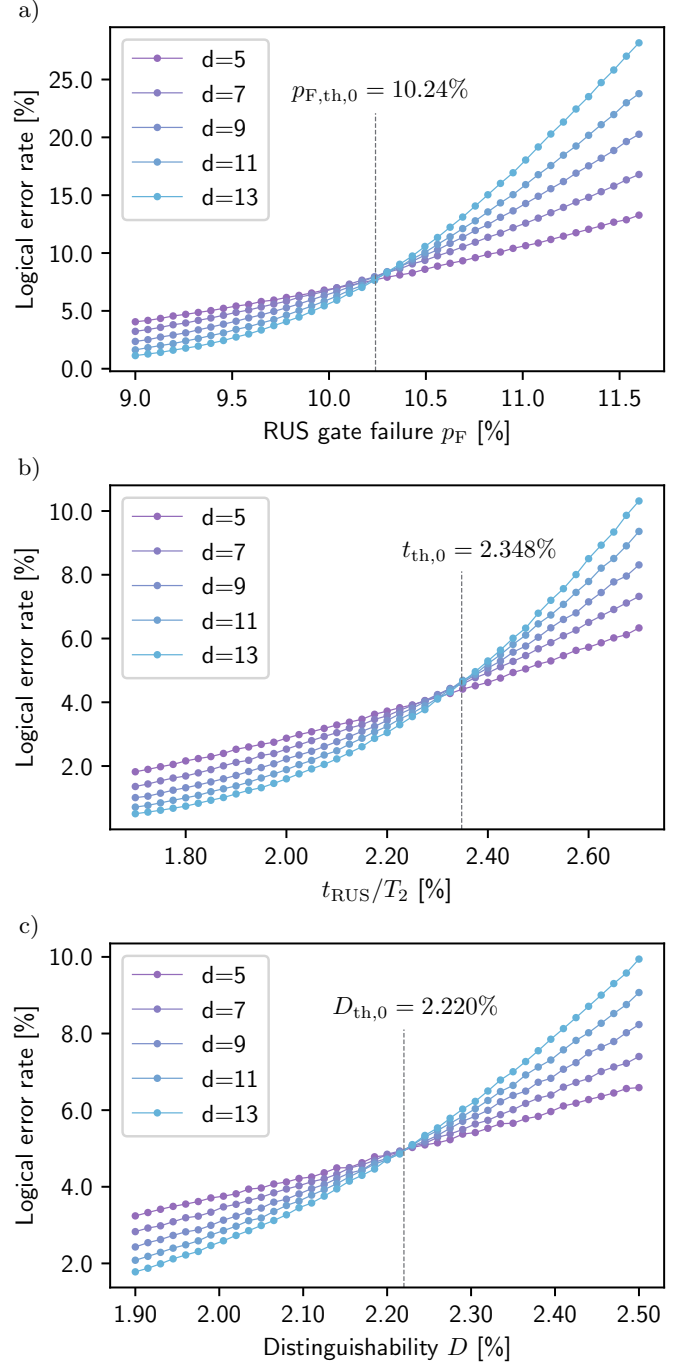


Figure 4. Logical error rate for different distance values vs (a) the RUS gate failure probability p_F , (b) the decoherence time of the spin t_{RUS}/T_2 , and (c) distinguishability of photons.

in Fig. 4 (b), assuming no photon losses ($p_F = 0$) and perfectly indistinguishable photons, we find the FT condition $t_{\text{RUS}}/T_2 < t_{\text{th},0} = 2.348 \pm 0.009\%$.

c. Distinguishable photons. Linear-optical entangling gates, such as RUS gates, heavily rely on having indistinguishable photonic qubits, i.e. photons that are indistinguishable in every degree of freedom other than

the one used for their qubit encoding. The presence of partially distinguishable photons introduces errors while performing the RUS gate – errors which could obviously hinder the computation. We let D denote the distinguishability between photons, assuming it to be the same for all photons from all emitters. The error channel caused by D is approximated by

$$C_{D,err}(\rho) := (1 - D)\rho + DC_{Z_a}C_{Z_b}(\rho)$$

and we refer interested readers to Appendix. B 2 for a detailed discussion on this result. Assuming no spin errors and no photon loss, we find that the SPOQC architecture can tolerate up to $D_{th,0} = 2.220 \pm 0.013\%$ of distinguishable photons, see Fig. 4 (c).

B. Multi-error RUS thresholds

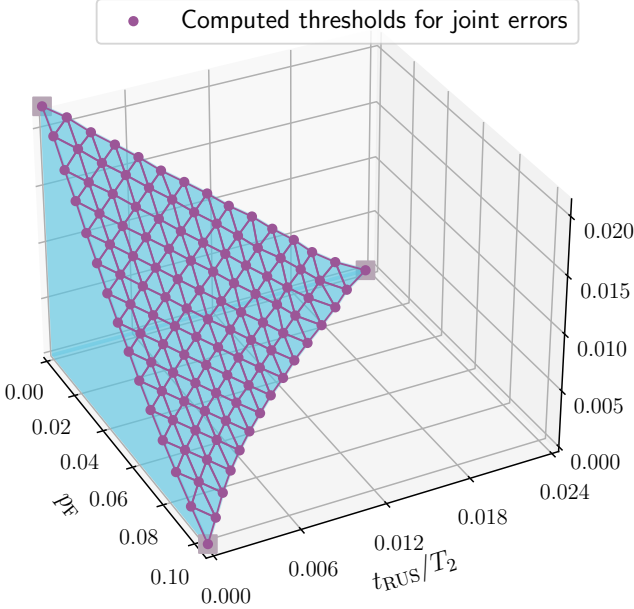


Figure 5. Fault-tolerant region for the SPOQC architecture in terms of t_{RUS}/T_2 , RUS gate failure p_F , and distinguishability D . The points highlighted with the light violet squares correspond to the individual error thresholds computed previously.

In the previous section, we have assumed independent errors: either solely loss, photon distinguishability, or decoherence. In practice, all errors can happen simultaneously and, intuitively, the more we have of one type of error the less we can correct of the other types. Given a vector of errors $\vec{m} = (t = t_{RUS}/T_2, p_F, D)$, we want to know whether it lies in the correctable region or not.

Through a numerical exploration detailed in Appendix C, we obtain the curve plotted in Fig. 5, which exhibits the correctable region (in light blue) for RUS gate failure, distinguishable photons, and spin decoherence time.

C. Physically relevant error threshold

1. With standard RUS gates

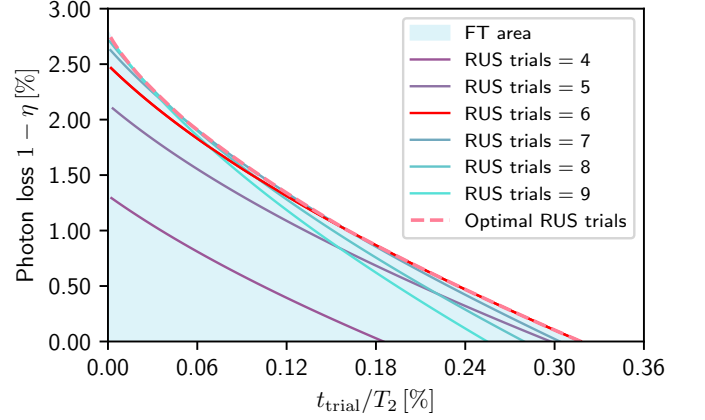


Figure 6. Fault-tolerant region of the SPOQC architecture in terms of t_{trial}/T_2 and single-photon loss ε as a function of the number k of trial of the RUS gates. The optimal curve corresponds to the maximum fault-tolerance optimized over k . The curve $k = 6$ is highlighted in red because it demonstrates remarkable balance between photon loss and decoherence time of the spin.

So far, we have exhibited the correctable region parameterized by the RUS gate parameters. Note that taking a larger number of trials k would result in a better single-photon loss tolerance. However, increasing k would also mean having significantly more stringent decoherence time requirements since the RUS gate total time would be larger. We aim at quantifying this interplay for the RUS gates as described in Section III.

To do so, we interpolate the border of the correctable area in Fig. 5 for a distinguishability $D = 0$. We use this curve to estimate, given a value of k and a single-photon loss $1 - \eta$, what is the maximum ratio $t_{th} = t_{RUS}/T_2$ tolerated by the architecture. From that, given a single-photon loss probability, we obtain straightforwardly the maximum trial time $t_{trial} = t_{th}/k$ allowed in order to remain in the FT regime. Repeating this for many k values results in finding the optimal FT region of loss and spin decoherence errors. The results are displayed in Fig. 6.

A first important conclusion that we can draw from Fig. 6 is that our scheme cannot be FT for values of k below 3. Indeed, even without loss the RUS gate fails or aborts with at least a probability 2^{-k} , and for $k \leq 3$, $p_{F,th,0} \leq 2^{-k}$. Therefore, it is impossible to reach the maximum RUS gate failure threshold if we do not allocate at least 4 trials per RUS gate.

A second important remark is that the optimal number of trials k depends on both the errors and their nature. Below the FT thresholds, systems more sensitive to photon loss would typically require larger number of trials k for their RUS gates than systems more sensitive

to spin decoherence. Also, even for small t_{trial}/T_2 , having $k \geq 8$ only marginally increases the loss tolerance, and the correctable area for $k = 6$ covers all of the correctable areas for smaller values of k and almost all the global FT region (a point is in the globally FT region if and only if for some k it is correctable) delimited by the optimal RUS trial curve.

We obtain that the SPOQC architecture can tolerate physical errors included in the FT area of Fig 6. With the rotated surface code, the SPOQC architecture tolerates up to $2.75 \pm 0.02\%$ photon loss and requires that a RUS gate trial time takes at most 0.318% of the decoherence time T_2 . However, it should be noted that the more photon loss the more trials are required to reach the loss threshold and thus the shorter we require each trial RUS gate to take compared to the spin decoherence time.

2. With hybrid RUS gates

As we emphasized by Fig. 6, RUS gates offer the best robustness against photon loss. However implementing a RUS gate can take a relatively long time as it requires sending photons one-by-one so the duration of each trial is the time of photon emission, transfer, and detection with additional time for classical processing and feedforward delays. This places stringent requirements on the spin coherence time. We investigate a slight relaxation of RUS gates where we allow the emitter to send multiple photons in a single trial. These photons will be processed by an adaptive linear-optical interferometer. This is detailed in Appendix D. We call these gates *hybrid* RUS gates. They are parameterized by the number of maximum trials k allowed and the number of photons n sent in each trial.

Again we investigate the interplay between photon loss and decoherence time of the spin, but this time for hybrid RUS gates. Results are shown in Figure 7. As expected we observe that at the expense of loss tolerance, we can drastically increase robustness to spin decoherence.

Note that the limit case for hybrid RUS gates in which we allow any number of photons and only one trial corresponds to boosted fusion gates [71] and that hybrid RUS gates with only one photon and many trials correspond to the standard RUS gates we introduced earlier.

V. COMPARISON WITH EXISTING ARCHITECTURES

Regarding comparison with other architectures, we should emphasize that a quantum emitter can have two roles, either as a carrier of quantum information or as a photon source.

Having a non-deterministic two-qubit gate is obviously a limitation compared to platforms with a full set of deterministic gates. Yet, using quantum emitters with long-range optical connections enables the use of non-local

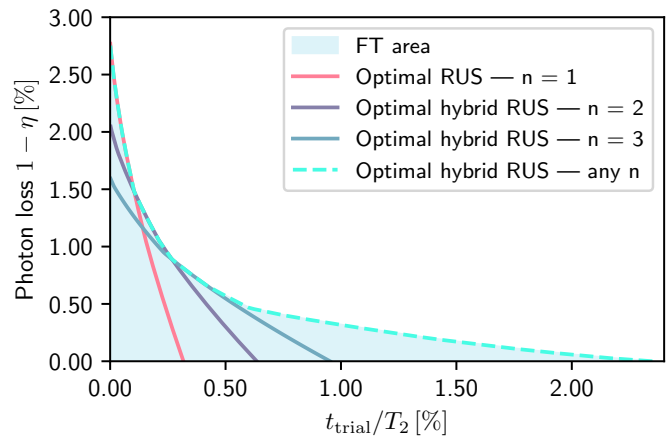


Figure 7. Fault-tolerant area of the SPOQC architecture in terms of t_{trial}/T_2 and single-photon loss ϵ for boosted fusion gates with varying number n of emitted photons n per trial. These curves have been optimised in the number of trials k .

links which could help in reducing the FTQC footprint by using high-encoding-rate LDPC codes [28, 29, 72–74]. Such codes require drastically less physical qubits per logical qubit compared to platforms with only local interaction. Indeed, non-local links between qubits allow for the use of *any* quantum LDPC code that could be appealing to implement, beyond just 2D or 3D codes. For example an impressive encoding rate of $k/n \rightarrow 13/72 \approx 0.18$, i.e. approximately 1 logical qubit for every 11 physical qubits (check qubits included) is known to be achievable [75].

Moreover, this architecture could significantly facilitate the error correction process through the use of single-shot error correction [50] and speed up the compilation process by implementing active volume strategies that rely on long-range interactions [51]. Furthermore, an architecture based on distant qubits could ensure a better isolation of each qubit, avoiding correlated noise, which is particularly detrimental for error correction [76, 77].

Recently, Ref. [78] proposed an architecture to produce a percolated graph state from quantum emitters using photonic probabilistic fusion gates and then renormalizing this graph into an interesting lattice. This scheme leads to a remarkable loss-tolerance threshold ($\approx 6\%$) and could also be envisioned using RUS gates. However, it also comes with the drawback of necessitating a renormalization step, which requires significant resource overhead and more stringent demands on the spin qubit coherence, control, and measurement performances. Indeed, errors in any quantum emitter measured out during the renormalization step may propagate to the data qubits and should thus increase the error rate that needs to be handled using quantum error correction.

Quantum emitters can also be embedded in photonic architectures, for example as a resource state generator in the fusion-based scheme of Ref. [14] and related all-photonic schemes [79, 80]. We reach similar loss tolerance ($1 - \eta_{\text{th},0} \approx 2.75\%$) to Ref. [14] when it uses the Shor(2,2)

6-ring resource state and much better performances compared to when it uses the non-encoded 4-star and 6-ring resource states. Moreover, while we achieve similar loss tolerance, the physical architecture is much simpler since the fusion-based architecture would require highly-reliable generation of Shor(2,2) 6-ring resource states, i.e. a 24-qubit photonic resource state with intrinsically small successful generation probability. Building complex resource states such as these cannot be realized deterministically with non-interacting quantum emitters [81]. To circumvent this issue, a resource state generator should heavily rely on multiplexing to ensure that a resource state is produced with arbitrarily high success probability. Such a resource state generator, even one based on quantum-emitter sources of entangled photons, could be quite resource intensive and would likely require complex optical setups. In comparison, the SPOQC architecture does not rely on multiplexing and thus requires comparably much simpler optical setups.

The original proposal for quantum computing using RUS gates [24, 54] also considered the generation of spin-based graph states, which can be used for FTQC. For example, Ref. [56] considered using probabilistic gates to build edges with high probability, resulting in a fault-tolerant 3D lattice. In that work, each vertex of the graph should correspond to a spin qubit. However, to increase its efficiency requires building a graph state of many spin qubits per vertex. In this respect, the proposal resembles the fusion-based architecture except that the resource state generator should prepare graph states of spin qubits instead of photons, with high success probability. Such an architecture leads to a much larger resource overhead since it requires multiplexing and more complex spin and optical setups compared to the relative simplicity of the SPOQC architecture.

VI. DISCUSSIONS

We have presented a modular fault-tolerant quantum computing architecture for quantum-emitter platforms based on photonic repeat-until-success gates. Contrary to most platforms with only nearest neighbor qubit links, here we can have arbitrary physical qubit connectivity since the two-qubit gates are made using photonic links. Therefore, this architecture is compatible with any QEC stabilizer code as it is organized around its Tanner graph, whose connectivity can be arranged with photonics. Furthermore, this architecture is scalable for the important class of LDPC codes.

Although we have presented the SPOQC architecture with quantum-dot emitters in mind [82], it can be made compatible with many other physical platforms [83]. In addition to atomic [15] and trapped-ion [16, 84] systems, this includes platforms based on proven spin-photon interfaces such as nitrogen-vacancy centers in diamond [61, 85] and emerging emitters like rare earth ions [86, 87] and silicon defects [88, 89]. The SPOQC ar-

chitecture may also be immediately applicable to many optically-active defects yet to be discovered in emerging materials like hexagonal boron-nitride [90–92]. Adapting SPOQC to the level structure of some of these emitters may require using a time-bin photonic qubit encoding [85].

In future work, we will explore directions for further enhancing the performance of the architecture. Adaptive strategies can improve the loss tolerance of architectures based on linear-optical gates [71, 93–95]. This has recently drastically improved the tolerance to photon loss probability of the fusion-based architecture of Ref. [14] from 2.7% to 7.5 %. We can expect to further improve the loss tolerance performance of the SPOQC architecture using similar strategies, for example by deciding whether or not to perform a probabilistic gate based on previous measurement outcomes. Moreover, in the current proposal, each RUS gate is performed sequentially and each gate takes a fixed number k of trials. However, these gates do not need to be performed sequentially: we do not need to wait to fully complete a first RUS gate between qubits a and b before starting making one between a and c . Instead, we can perform them “in parallel”. Besides, instead of having a fixed number of trials per RUS gate, we can, in principle, dynamically allocate the trials to multiple gates and we can envision requiring fewer trials for similar performances: if a RUS gate succeeds, we can dynamically allocate its remaining trials to another gate. We expect this strategy to reduce the time it takes to perform a full error correction cycle and thus be less sensitive to spin decoherence. These are three potential routes for further investigations and improvements of this architecture.

ACKNOWLEDGMENTS

We thank Boris Bourdoncle for fruitful discussions throughout the entire project. We thank Sharon David and Théo Dessertaine, who helped us to spot an error in the simulations and Théo Dessertaine, Nils Ottink, and Nathan Coste for their careful revision of the paper. We appreciate Elina Kostanian’s assistance in enhancing the visual rendering of the figures. Live long and prosper. 🙌

AUTHOR CONTRIBUTIONS

G.G. and P.H. contributed equally to this work. P.H. proposed the main architecture ideas, wrote the paper and contributed to the visualization and to the simulations. G.G. contributed to the main architecture ideas, to visualization, to simulation, to research on the decoder and to the paper writing. P-E.E. wrote the paper, contributed to visualization and to the simulations and participated to conceptualization. S.C.W. contributed to the physical noise models and edited the paper. A.S.

contributed to research on the decoder and discussions on the code and draft. S.M. supervised.

Appendix A: Discussion on the scalability of SPOQC with non-local LDPC codes

Strictly speaking, implementing a non-local LDPC code using this architecture cannot be a scalable architecture since it requires quantum channels that increase with the computer's size, and thus increase time latencies and fiber losses. Investigating long-range code, comes with significant benefits in terms of reducing resource overhead [96–98] and should still be considered. As long as the time latencies and the fiber loss do not become the principal source of errors, such FTQC architecture could have a practical interest.

Relaxing this requirement is sound as long as the overhead it caused is small compared to other source of errors. In particular, for fiber loss, given that a qubit module has a spatial footprint of V , and that we can use a D -dimensional qubit arrangement ($D \leq 3$ for a spatial layout compatible with our space-time), the losses scales in principle with $\propto e^{-N^{1/D}(V^{1/3}/L_{\text{att}})}$ with N the number of qubits in the FT quantum computer and L_{att} the channel attenuation length. This typical loss should be much smaller than the loss thresholds, which is all the easier to achieve for platforms with spatial footprint $V \ll L_{\text{att}}^3$. For telecom photons, the typical attenuation distance of a fiber is of the order of 22 km, and we can also envision free-space optical links if need be [51].

Appendix B: Physical noise models

1. Realistic modeling of the relaxation and dephasing of a quantum emitter

A quantum emitter can be seen as a quantum memory (its spin), that can be interfaced with photons. How-

ever, due to its interaction with its environment, this spin qubit cannot store quantum information for an infinitely long time. In practice, due to its interaction with the environment, it is limited by its relaxation time and its coherence time, respectively denoted T_1 and T_2 .

Let $\hbar\omega_{\uparrow\downarrow}$ be the energy splitting between the lower-energy $|\downarrow\rangle$ spin state and the higher-energy $|\uparrow\rangle$ spin state. If $\hbar\omega_{\uparrow\downarrow}$ is much larger than the temperature of the environment $k_B T$, then the qubit will relax to the state $|\downarrow\rangle$. However, in the opposite limit $\hbar\omega_{\uparrow\downarrow} \ll k_B T$, the qubit will relax towards a completely mixed spin state. A simple model of qubit relaxation due to a thermal bath is described by a Lindblad master equation $d\rho(t)/dt = \mathcal{L}\rho(t)$ [99] where the generator is

$$\begin{aligned} \mathcal{L}\rho = & -\frac{i}{\hbar} [H, \rho] + \gamma_0(n_{\text{th}}(T) + 1)\mathcal{D}(\sigma_-)\rho \\ & + \gamma_0 n_{\text{th}}(T)\mathcal{D}(\sigma_+)\rho(t) + \frac{\gamma^*(T)}{2}\mathcal{D}(\sigma_z)\rho \end{aligned} \quad (\text{B1})$$

and where $H = \hbar\omega_{\uparrow\downarrow}\sigma_z/2$ is the spin qubit Hamiltonian, $\sigma_z = |\uparrow\rangle\langle\uparrow| - |\downarrow\rangle\langle\downarrow|$ is the Pauli-Z operator, $\sigma_- = |\downarrow\rangle\langle\uparrow|$ is the spin lowering operator, $\sigma_+ = |\uparrow\rangle\langle\downarrow|$ is the spin raising operator, γ_0 is the zero-temperature relaxation rate defined by the spin-bath coupling strength, $n_{\text{th}}(T) = 1/(e^{\hbar\omega_{\uparrow\downarrow}/k_B T} - 1)$ is the thermal population of the bath, and $\gamma^*(T)$ is the spin pure dephasing rate at temperature T . The non-Hermitian evolution is governed by the Lindblad dissipator defined by

$$\mathcal{D}(L)\rho = L\rho L^\dagger - \frac{1}{2}L^\dagger L\rho - \frac{1}{2}\rho L^\dagger L. \quad (\text{B2})$$

The noise channel C_t acting on the qubit for a duration of time t is the general solution to the Lindblad master equation: $dC_t/dt = \mathcal{L}C_t$ in the frame rotating with the spin qubit precession. Since the generator \mathcal{L} is time-independent, the solution is given by $C_t = e^{t\mathcal{L}}$, which can be analytically solved by diagonalising \mathcal{L} to obtain

$$\begin{aligned} C_t(\rho) = & \frac{1}{(\gamma_\downarrow + \gamma_\uparrow)} \left[\left(\gamma_\downarrow + \gamma_\uparrow e^{-t(\gamma_\downarrow + \gamma_\uparrow)} \right) \rho_{\uparrow\uparrow}\rho\rho_{\uparrow\uparrow} + \left(\gamma_\uparrow + \gamma_\downarrow e^{-t(\gamma_\downarrow + \gamma_\uparrow)} \right) \rho_{\downarrow\downarrow}\rho\rho_{\downarrow\downarrow} \right. \\ & + \gamma_\uparrow \left(1 - e^{-t(\gamma_\downarrow + \gamma_\uparrow)} \right) \rho_{\downarrow\downarrow}\rho\rho_{\uparrow\uparrow} + \gamma_\downarrow \left(1 - e^{-t(\gamma_\downarrow + \gamma_\uparrow)} \right) \rho_{\uparrow\uparrow}\rho\rho_{\downarrow\downarrow} \\ & \left. (\gamma_\downarrow + \gamma_\uparrow) e^{-t((\gamma_\downarrow + \gamma_\uparrow)/2 - \gamma^*)} (\rho_{\downarrow\uparrow}\rho\rho_{\uparrow\downarrow} + \rho_{\uparrow\downarrow}\rho\rho_{\downarrow\uparrow}) \right] \end{aligned} \quad (\text{B3})$$

where $\rho_{ij} = |i\rangle\langle j|$, $\gamma_\uparrow = \gamma_0 n_{\text{th}}(T)$, and $\gamma_\downarrow = \gamma_0(n_{\text{th}}(T) + 1)$. This channel is not a Pauli channel in general. However, in the limit that $n_{\text{th}} \gg 1$ (or where $\hbar\omega \ll k_B T$), we have $\gamma_\uparrow \simeq \gamma_\downarrow = \gamma$. In this case, we can

write

$$C_t(\rho) = (1 - p_X - p_Y - p_Z)\rho + p_X X\rho X + p_Y Y\rho Y + p_Z Z\rho Z \quad (\text{B4})$$

where

$$\begin{aligned} p_X &= p_Y = \frac{1 - e^{-2t\gamma}}{4} \\ p_Z &= \frac{1 - e^{-t(\gamma+\gamma^*)}}{2} - \frac{1 - e^{-2t\gamma}}{4}. \end{aligned} \quad (\text{B5})$$

This is a Pauli error channel where the effective relaxation time is $T_1 = 1/2\gamma$, the coherence time is $T_2 = 1/(\gamma + \gamma^*)$, and we have that $T_2 \leq 2T_1$.

2. Partial photon distinguishability

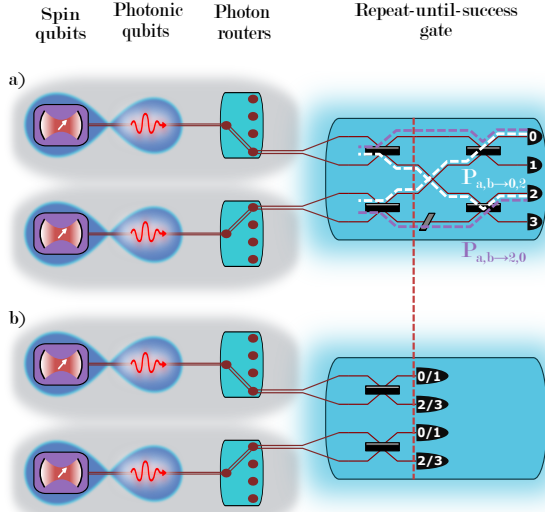


Figure 8. (a) Linear-optical interferometer with input spin quantum emitters. The paths $P_{a,b \rightarrow 0,2}$ and $P_{a,b \rightarrow 2,0}$ are represented in white and violet dashed lines respectively. The vertical red dashed line corresponds to the zone before the mode swap mentioned in the main text. (b) “Equivalent” linear-optical interferometer for distinguishable photons.

Photons emitted by two different quantum emitters should interfere together on a linear-optical interferometer. These photons should thus be perfectly indistinguishable to lead to a unity fidelity RUS gate. The photon indistinguishability is denoted by M and is equal to 1 for perfectly indistinguishable photons, and 0 for completely distinguishable photons (which cannot interfere together). This quantity corresponds to the overlap of the wavefunctions of two single photons and can be calculated experimentally with a Hong-Ou-Mandel experiment [100]. We are interested in the partial distinguishability $D = 1 - M$ which corresponds to an error afflicting our system. For simplicity, we consider that this distinguishability afflicts identically all the photons emitted by all the quantum emitters.

Having photon indistinguishability is detrimental for the RUS gate and we want to evaluate its impact. Physically, it forbids the erasure of the photon “which-path”

information that is at the core of linear-optical gates. A path corresponds to the trajectories of photons into the interferometers to the detectors. For example “photons a and b , respectively emitted by quantum emitters a and b , are respectively detected in mode 0 and 2” is a path, that we call path $P_{a,b \rightarrow 0,2}$, see Fig. 8(a).

We can have a second path $P_{a,b \rightarrow 2,0}$ “photons a and b , respectively emitted by a and b , are respectively detected in mode 2 and 0”. These two paths are not identical, $P_{a,b \rightarrow 0,2} \neq P_{a,b \rightarrow 2,0}$, but have the same detection pattern (0, 2). For indistinguishable photons, given the detection pattern (0, 2), it is physically impossible to know which path the photons have followed, hence the name of which-path information erasure, which can lead to interference between these paths and linear-optical entangling gates. However, If we have distinguishable photons, it is possible, in theory, to identify in which detector photon a has been detected. In this example, this means that it is possible to know whether the photons have followed path $P_{a,b \rightarrow 0,2}$ or path $P_{a,b \rightarrow 2,0}$. While we don’t have access to this information, this leads to the absence of entangling gate and a statistical mixture of these two paths.

For distinguishable photons, if we were able to discriminate them at the detector, we could easily retrieve their path up to before the mode swapping (see the dashed red line in Fig. 8(a)). Therefore, the distinguishable case corresponds to the linear-optical interferometer in Fig. 8(b), which perform a photon X measurement in the photonic qubit basis.

a. Repeat detection pattern For partial failure detection pattern, the effect on the spin is similar whether or not we have distinguishable or indistinguishable photons. Indeed, we can identify which path each photon has followed in a partial failure so there are no which-path information erasure. Therefore, we should only focus on the successful detection patterns. For distinguishable photons, we can also obtain the detection patterns (0, 1) and (2, 3). These cases are impossible with indistinguishable photons because they are forbidden by the Hong-Ou-Mandel interference on the last beamsplitters of the linear-optical interferometer. For the same reasons as before, these patterns are well handled and do not lead to additional errors induced by distinguishable photons.

b. Successful detection pattern For indistinguishable photons, successful detection patterns perform a CZ gate on the spin qubits up to some correction unitary C that depends on the detection pattern. We focus on the detection pattern (0, 2), for which $C = S_a S_b^\dagger$, but the same reasoning can be applied to any successful detection pattern. For distinguishable photons, following path $P_{a,b \rightarrow 0,2}$ (respectively $P_{a,b \rightarrow 2,0}$) corresponds to a measurement of the photons in the $|+_a, -_b\rangle$ state (respectively $|-_a, +_b\rangle$). This corresponds to applying a unitary Z_b (respectively Z_a) on the spin states. However, in practice we don’t know that the photons were distinguishable, and we don’t know which path has been followed. Therefore, we perform the correction C on a statistical mixture of the two paths. Therefore, for partially distinguishable

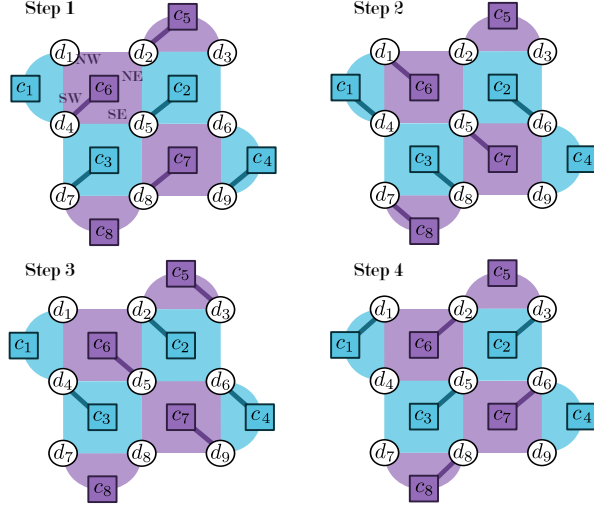


Figure 9. Illustration of the order in which the RUS CZ are performed. Thick edges corresponds to a CZ gate being performed at a given step.

photons, we perform the channel:

$$C_D(\rho) = (1 - D)CZ_{a,b}\rho CZ_{a,b} + \frac{D}{2}S_a S_b^\dagger (Z_a \rho Z_a + Z_b \rho Z_b) S_a^\dagger S_b.$$

We can rewrite this as the desired gate channel, followed by the error channel:

$$C_D(\rho) = C_{D,err}(CZ_{a,b}\rho CZ_{a,b})$$

with

$$C_{D,err}(\rho) = (1 - D)\rho + \frac{D}{2}CZ_{a,b}(S_a S_b \rho S_a^\dagger S_b^\dagger + S_a^\dagger S_b^\dagger \rho S_a S_b)CZ_{a,b}.$$

Because, this channel is not a Pauli error channel, we simplify it by amplifying the noise into a completely dephasing channel. By doing so, we overestimate the effect of distinguishability by considering the channel:

$$C_{D,err}(\rho) \rightarrow C_{RUS,s}(\rho) = (1 - D)\rho + DC_{Z_a}C_{Z_b}(\rho)$$

with

$$C_{Z_i}(\rho) = \frac{1}{2}(\rho + Z_i \rho Z_i).$$

Appendix C: Notes on the numerical simulations

1. Simulation details

Here, we give some details about the way we perform the numerical simulations. We used Stim [66] to carry

out efficient stabilizer simulations and Pymatching [67] for the minimum-weight perfect matching decoder.

To measure the stabilizers, we use a noisy indirect stabilizer measurement circuit as was presented in Fig. 2. However, instead of performing each stabilizer measurement one after the other, we perform them “all at once”. This avoid the unnecessary propagation of errors. We use the strategy proposed in [101] and illustrated in Fig. 9. The edges connecting a check qubit are oriented along the North West (NW, e.g. edge (c_6, d_1)), North East (NE, e.g. (c_6, d_2)), South East (SE, e.g. (c_6, d_5)) and South West (SW, e.g. (c_6, d_4)) directions. We perform the CZ gates in four steps illustrated in Fig. 9: for X-type (respectively Z-type) stabilizers, we start by SW, then NW, SE, and finally NE (respectively, SW, SE, NW, and then NE) CZ gates. This way one full cycle of syndrome measurements only takes the time of four entangling steps and do not depend on the distance d of the rotated surface code.

Instead of a theoretical CZ gate, we perform a RUS CZ gate, which can either succeed, fail or abort and be heralded. For the simulations, we consider the abort and failure cases with the same error channel $C_{RUS,f}(\rho)$. This channel corresponds to the failure case, while there are a priori no phase erasure in the case of the abort case. Therefore, this assumption leads to an overestimate of the error made in the case of an aborted case but also simplify the analysis as was detailed in the main manuscript.

Heralded error in Stim. Stim did not take into account heralded errors natively when the simulations were performed. To account for the fact that this gate is heralded in Stim, we consider the use of an extra ancilla qubit c . For a CZ gate between qubit a and b , we use the ancilla qubit c , initialized in the $|0\rangle$ state, as:

$$C_{RUS}(\rho_{ab} \otimes |0\rangle\langle 0|_c) = (1 - p_F)C_{RUS,s}(\rho_{ab}) \otimes |0\rangle\langle 0|_c + p_F C_{RUS,f}(\rho_{ab}) \otimes X_c |0\rangle\langle 0|_c X_c. \quad (C1)$$

We then measure qubit c , if it has not been flipped, it succeeded and the successful gate has been applied. Otherwise, $X_c |0\rangle\langle 0|_c X_c = |1\rangle\langle 1|_c$, we have applied the unsuccessful gate.

Moreover, since $C_{RUS,f}(\rho)$ is the two-qubit completely dephasing channels, $C_{RUS,f}C_{RUS,s}(\rho) = C_{RUS,f}(\rho)$, therefore we can rewrite Eq. (C1) as

$$C_{RUS}(\rho_{ab} \otimes |0\rangle\langle 0|_c) = C_{RUS,f,err}(C_{RUS,s}(\rho_{ab}) \otimes |0\rangle\langle 0|_c)$$

with

$$C_{RUS,f,err}(\rho_{ab} \otimes |0\rangle\langle 0|_c) = (1 - p_F)\rho_{ab} \otimes |0\rangle\langle 0|_c + p_F C_{RUS,f}(\rho_{ab}) \otimes |1\rangle\langle 1|_c. \quad (C2)$$

This “hack” allows accounting for heralded errors in Stim [102].

Decoding heralded errors. We used Pymatching’s minimum weight perfect matching (MWPM) decoder [67]. The latter works together with Stim [66] that determines a detector error model, namely the error model

on the check operators measured during the simulations. Pymatching builds a graph out of it, and applies the MWPM algorithm on it. This Stim/Pymatching interfacing allows keeping track of errors efficiently and automatically, even with complex error models. However, heralded errors are not natively taken into account through this interfacing. To address this issue, we start by performing a simulation without heralded errors and extract its detector error model. Depending on the heralding information received during the simulations, we update this initial detector error model to account for these heralded errors. This corresponds to updating the matching graph accordingly as was done for example in Ref. [69]. In this work, qubit erasures were incorporated with simple updates on the matching graph, however heralded RUS gates failure usually result in correlated errors and the updates are not simple to determine. To deal with such errors, we pre-compute a register of error model for each heralded gate of a circuit, which we can build once and store prior to the simulations and use whenever needed for a given simulation. To build this register, we perform one simulation per heralded error which are error-less except for this specific error. We can thus extract its corresponding detector error model. This way of handling errors may not be the most efficient but it is sufficient for our current needs and is very versatile as it can be used in theory for any type of heralded errors, not simply to qubit erasures: even partial erasure can be handled in this case which could have practical applications for other platforms where similar strategies can be used [103].

Spin dephasing. The last type of errors accounted for in our simulations are spin decoherence errors that lead to a continuous time error $C_t(\rho)$ from Eq. (B4). Assuming $T_2 \ll T_1$, and taking $T_1 \rightarrow \infty$, this channel has the form of a dephasing channel:

$$C_t(\rho) = (1 - p_Z)\rho + p_Z Z\rho Z.$$

with p_Z depending on t . We consider all the decoherence to occur for a time $t = t_{\text{RUS}}$ before each of the 4 time steps discussed previously. We can do this since the spin decoherence channel commutes with all the RUS gate channels. A full error correction cycle thus lasts $4t_{\text{RUS}}$ assuming that all the other operation takes negligible time compared to a RUS gate.

We also consider that we can perform any single-qubit operation and measurement with unit fidelity. We leave more complete error model to further study.

2. Numerical results for independent errors

For all the numerical simulations, we evaluate the error threshold by performing a fault tolerant initialization of the logically-encoded qubit. For a $[[d^2, 1, d]]$ rotated surface code, we start with n disentangled physical qubits in the state $|0\rangle^{\otimes n}$ (respectively $|+\rangle^{\otimes n} = (|0\rangle + |1\rangle)^{\otimes n}$) and we want to encode a logical $|0\rangle_L$ (respectively $|+\rangle_L$)

qubit using noisy gates and qubits. We do so by performing d cycles of error correction and then we measure all the qubits in the Z (respectively X) basis to evaluate whether or not the fault-tolerant initialization was successful: if the measurement gives $|1\rangle_L$ (respectively $|-\rangle_L = |0\rangle_L - |1\rangle_L$), we have a logical error.

3. Determination of the fault-tolerant region of errors

We wish to explore a tri-dimensional parameter space corresponding to the three main physically relevant errors that occurs in a SPOQC architecture: photon loss, partial distinguishability, and the spin decoherence time. We would like to extract the border between the FT regime and the non-FT regime. This border corresponds to a surface S in this tri-dimensional space.

We already know three points from S consecutive to the study of individual errors: $\vec{OA} = (p_{\text{F,th},0}, 0, 0)$, $\vec{OB} = (0, t_{\text{th},0}, 0)$, and $\vec{OC} = (0, 0, D_{\text{th},0})$.

To reduce the parameter space exploration, we make the assumption that the border S is “not too far” from the plane \hat{S} passing by these three points and defined by the equation $\frac{x}{p_{\text{F,th},0}} + \frac{y}{t_{\text{th},0}} + \frac{z}{D_{\text{th},0}} = 1$. We verify that this assumption is sound later on through the simulations.

To find the correct surface S , we first start by taking a tessellation of points on the plane \hat{S} (more precisely on the intersection of this plane with $(\mathbb{R}^+)^3$). For each point M , we consider the line ℓ_M passing through the origin O defined by the vector \vec{OM} and want to identify the intersection point N of ℓ_M with the real FT-threshold surface S . The line ℓ_M is parameterized by $\vec{OM}'(w) = w\vec{OM}$ and we look for the value w_{th} corresponding to the intersection of ℓ_M with the surface S . We do so by performing simulations for combined errors corresponding to $w\vec{OM}$ on the error space. The error intensities all increase with w and we identify the FT threshold corresponding to the crossing points between two curves of distance d and $d+2$ as a function of w . We use $d = 11$ in our simulations. This crossing point is w_{th} corresponding to the real crossing point between ℓ_M and S . The assumption that S is close to the planar surface \hat{S} helps us in using a small interval $[w_{\text{min}}, w_{\text{max}}]$ of values close to 1 to avoid exploring the full error space. After a first refinement, we use an interval $[w_{\text{min}}, w_{\text{max}}] = [0.85, 1]$ and ensure that the assumption is valid by checking that w_{th} is always found within $[w_{\text{min}}, w_{\text{max}}]$. To obtain the border S in Fig. 5, we plot the thresholds point that we have found along each lines ℓ_M of the tessellation of $n_p = 120$ points.

Appendix D: Variant with hybrid RUS gates

The RUS gate offers the best robustness against photon loss, but as we can see in Fig. 6, the need of using many trials causes stringent requirements on the spin

coherence time. A RUS gate is indeed relatively long as it requires to store quantum information on the spins for k trials corresponding to the time of photon emission, transfer, and detection and also from the classical processing and feedforward delays.

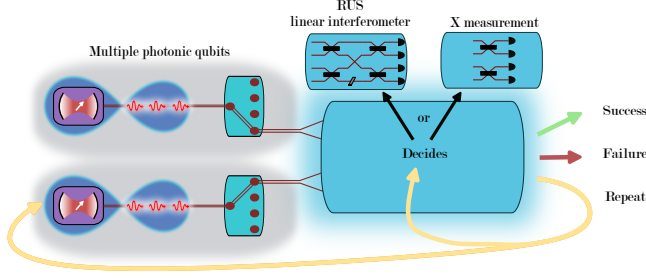


Figure 10. Hybrid RUS gate including spin qubits capable of emitting multiple entangled photons, an adaptive interferometer and detectors. The linear-optical interferometer is adaptive and depends on previous measurement outcomes. Horizontal black rectangles correspond to 50 : 50 beam splitter, the inclined parallelogram corresponds to a $-\pi/2$ phase shifter, numbered semiovals are photon-number-resolving detectors.

An alternative strategy relies on boosted fusion gates [71] and is potentially much faster as it requires only one trial step. Contrary to a RUS gate where only one photon is sent per trial, each spin emits sequentially n photons that will be processed by an adaptive linear-optical interferometer. Depending on the previous measurement outcomes, the linear-optical interferometer corresponds either to the one of a RUS gate (if no previous measurements has yielded a successful detection pattern) or it corresponds to two independent X measurements on the photonic qubits. Fig. 10 illustrates a physical implementation of such a gate. We can picture this as making the $k = n$ trials of an equivalent RUS gate “all at once”, that is, n trials of the RUS gate is implementing by a hybrid RUS gates with n photons per trial, provided that no photon is lost.

Interestingly, all the results derived in the paper are valid if we replace RUS gates by hybrid RUS gates that is if we replace the building block based on single-photon emission with a hybrid gate based on multiple sequential photon emissions. If we consider this hybrid scheme, hereafter denoted as $\text{HRUS}(k, n)$ for at most k trials with n photons per trial, we can increase the fault-tolerant region of our architecture.

$\text{HRUS}(k, n)$ is successful if we obtained at least one correct detection pattern *and* if all the emitted photons have been successfully detected:

$$p_s = (1 - 2^{-n})(\eta_a \eta_b)^n.$$

The hybrid gate has failed if at least one photon is lost:

$$p_f = 1 - (\eta_a \eta_b)^n,$$

and it has been aborted otherwise:

$$p_r = 2^{-n}(\eta_a \eta_b)^n.$$

In that case, the total success, failure and abort probabilities are given by

$$\begin{aligned} P_{\text{HRUS},s}(\eta_a, \eta_b, k, n) &= p_s \sum_{j=0}^{k-1} p_r^j, \\ P_{\text{HRUS},f}(\eta_a, \eta_b, k, n) &= p_f \sum_{j=0}^{k-1} p_r^j, \\ P_{\text{HRUS},a}(\eta_a, \eta_b, k, n) &= 1 - P_{\text{HRUS},s}(\eta_a, \eta_b, k, n) \\ &\quad - P_{\text{HRUS},f}(\eta_a, \eta_b, k, n). \end{aligned}$$

Note that a $\text{HRUS}(k, 1)$ is identical to the standard RUS gate we have introduced in Section III and a $\text{HRUS}(1, n)$ gate is equivalent to a boosted fusion gate [71].

Compared to RUS gates, HRUS gates (with $n \geq 2$) have a lower maximum success rate in the presence of loss than RUS gates. Yet, they are also faster as they usually require less trials. They should thus yield better performances when the spin coherence time is the critical figure of merit. In the main manuscript, we have assumed that a single trial of RUS or HRUS gate takes the same amount of time irrelevant of the number of photons n being emitted per trial. This assumption holds for typically small number of photons and whenever the emission process is fast compared to the feedforward delay time in between trials.

-
- [1] Dorit Aharonov and Michael Ben-Or. Fault-tolerant quantum computation with constant error. In *Proceedings of the twenty-ninth annual ACM symposium on Theory of computing*, pages 176–188, 1997.
 - [2] Emanuel Knill, Raymond Laflamme, and Wojciech H Zurek. Resilient quantum computation. *Science*, 279(5349):342–345, 1998.
 - [3] A Yu Kitaev. Fault-tolerant quantum computation by anyons. *Annals of physics*, 303(1):2–30, 2003.
 - [4] Adriano Barenco, Charles H Bennett, Richard Cleve, David P DiVincenzo, Norman Margolus, Peter Shor, Tycho Sleator, John A Smolin, and Harald Weinfurter. Elementary gates for quantum computation. *Physical review A*, 52(5):3457, 1995.
 - [5] Robert Raussendorf and Hans J Briegel. A one-way quantum computer. *Physical review letters*, 86(22):5188, 2001.
 - [6] Janet Anders, Daniel KL Oi, Elham Kashefi, Dan E Browne, and Erika Andersson. Ancilla-driven universal quantum computation. *Physical Review A*, 82(2):020301, 2010.
 - [7] Arnab Das and Bikas K Chakrabarti. Colloquium: Quantum annealing and analog quantum computation. *Reviews of Modern Physics*, 80(3):1061, 2008.
 - [8] Rodney Van Meter, Thaddeus D Ladd, Austin G Fowler, and Yoshihisa Yamamoto. Distributed quantum computation architecture using semiconductor nanophotonics. *International Journal of Quantum Information*, 8(01n02):295–323, 2010.
 - [9] Christopher Monroe, Robert Raussendorf, Alex Ruthven, Kenneth R Brown, Peter Maunz, L-M Duan, and Jungsang Kim. Large-scale modular quantum-computer architecture with atomic memory and photonic interconnects. *Physical Review A*, 89(2):022317, 2014.
 - [10] Naomi H Nickerson, Joseph F Fitzsimons, and Simon C Benjamin. Freely scalable quantum technologies using cells of 5-to-50 qubits with very lossy and noisy photonic links. *Physical Review X*, 4(4):041041, 2014.
 - [11] Hector Bombin, Isaac H Kim, Daniel Litinski, Naomi Nickerson, Mihir Pant, Fernando Pastawski, Sam Roberts, and Terry Rudolph. Interleaving: Modular architectures for fault-tolerant photonic quantum computing. *arXiv preprint arXiv:2103.08612*, 2021.
 - [12] J Eli Bourassa, Rafael N Alexander, Michael Vasmer, Ashlesha Patil, Ilan Tzitrin, Takaya Matsuura, Daiqin Su, Ben Q Baragiola, Saikat Guha, Guillaume Dauphinais, et al. Blueprint for a scalable photonic fault-tolerant quantum computer. *Quantum*, 5:392, 2021.
 - [13] Christopher Chamberland, Kyungjoo Noh, Patricio Arrangoiz-Arriola, Earl T Campbell, Connor T Hann, Joseph Iverson, Harald Putterman, Thomas C Bohdanowicz, Steven T Flammia, Andrew Keller, et al. Building a fault-tolerant quantum computer using concatenated cat codes. *PRX Quantum*, 3(1):010329, 2022.
 - [14] Sara Bartolucci, Patrick Birchall, Hector Bombin, Hugo Cable, Chris Dawson, Mercedes Gimeno-Segovia, Eric Johnston, Konrad Kieling, Naomi Nickerson, Mihir Pant, et al. Fusion-based quantum computation. *Nature Communications*, 14(1):912, 2023.
 - [15] Philip Thomas, Leonardo Ruscio, Olivier Morin, and Gerhard Rempe. Efficient generation of entangled multiphoton graph states from a single atom. *Nature*, 608(7924):677–681, 2022.
 - [16] Boris B Blinov, David L Moehring, L-M Duan, and Chris Monroe. Observation of entanglement between a single trapped atom and a single photon. *Nature*, 428(6979):153–157, 2004.
 - [17] Ido Schwartz, Dan Cogan, Emma R Schmidgall, Yaroslav Don, Liron Gantz, Oded Kenneth, Netanel H Lindner, and David Gershoni. Deterministic generation of a cluster state of entangled photons. *Science*, 354(6311):434–437, 2016.
 - [18] N Coste, DA Fioretto, N Belabas, SC Wein, P Hilaire, R Frantzeskakis, M Gundin, B Goes, N Somaschi, M Morassi, et al. High-rate entanglement between a semiconductor spin and indistinguishable photons. *Nature Photonics*, pages 1–6, 2023.
 - [19] Dan Cogan, Zu-En Su, Oded Kenneth, and David Gershoni. Deterministic generation of indistinguishable photons in a cluster state. *Nature Photonics*, pages 1–6, 2023.
 - [20] Yijian Meng, Ming Lai Chan, Rasmus B Nielsen, Martin H Appel, Zhe Liu, Ying Wang, Nikolai Bart, Andreas D Wieck, Arne Ludwig, Leonardo Midolo, et al. Deterministic photon source of genuine three-qubit entanglement. *arXiv preprint arXiv:2310.12038*, 2023.
 - [21] Paul Hilaire, Leonid Vidro, Hagai S Eisenberg, and Sophia E Economou. Near-deterministic hybrid generation of arbitrary photonic graph states using a single quantum emitter and linear optics. *Quantum*, 7:992, 2023.
 - [22] Christian Schön, Enrique Solano, Frank Verstraete, J Ignacio Cirac, and Michael M Wolf. Sequential generation of entangled multiqubit states. *Physical review letters*, 95(11):110503, 2005.
 - [23] Netanel H Lindner and Terry Rudolph. Proposal for pulsed on-demand sources of photonic cluster state strings. *Physical review letters*, 103(11):113602, 2009.
 - [24] Yuan Liang Lim, Almut Beige, and Leong Chuan Kwek. Repeat-until-success linear optics distributed quantum computing. *Physical review letters*, 95(3):030505, 2005.
 - [25] Nicolas Heurtel, Andreas Fyrrillas, Grégoire de Glinasty, Raphaël Le Bihan, Sébastien Malherbe, Marc Pailhas, Eric Bertasi, Boris Bourdoncle, Pierre-Emmanuel Emeriau, Rawad Mezher, et al. Perceval: A software platform for discrete variable photonic quantum computing. *Quantum*, 7:931, 2023.
 - [26] Hector Bombin and Miguel Angel Martin-Delgado. Topological quantum distillation. *Physical review letters*, 97(18):180501, 2006.
 - [27] Nikolas P Breuckmann and Jens Niklas Eberhardt. Quantum low-density parity-check codes. *PRX Quantum*, 2(4):040101, 2021.
 - [28] Anthony Leverrier and Gilles Zémor. Quantum tanner codes. In *2022 IEEE 63rd Annual Symposium on Foundations of Computer Science (FOCS)*, pages 872–883. IEEE, 2022.
 - [29] Pavel Panteleev and Gleb Kalachev. Asymptotically good quantum and locally testable classical ldpc codes. In *Proceedings of the 54th Annual ACM SIGACT Symposium on Theory of Computing*, pages 375–388, 2022.

- [30] Note1. see Appendix A for a more detailed discussion on the scalability for non-local LDPC code.
- [31] Daniel Litinski. A game of surface codes: Large-scale quantum computing with lattice surgery. *Quantum*, 3: 128, 2019.
- [32] Sergey Bravyi and Alexei Kitaev. Universal quantum computation with ideal clifford gates and noisy ancillas. *Physical Review A*, 71(2):022316, 2005.
- [33] Clare Horsman, Austin G Fowler, Simon Devitt, and Rodney Van Meter. Surface code quantum computing by lattice surgery. *New Journal of Physics*, 14(12): 123011, 2012.
- [34] Jonas T Anderson, Guillaume Duclos-Cianci, and David Poulin. Fault-tolerant conversion between the steane and reed-muller quantum codes. *Physical review letters*, 113(8):080501, 2014.
- [35] Dave Bacon. Operator quantum error-correcting subsystems for self-correcting quantum memories. *Physical Review A*, 73(1):012340, 2006.
- [36] Matthew B Hastings and Jeongwan Haah. Dynamically generated logical qubits. *Quantum*, 5:564, 2021.
- [37] Alex Townsend-Teague, Julio Magdalena de la Fuente, and Markus Kesselring. Floquetifying the colour code. *arXiv preprint arXiv:2307.11136*, 2023.
- [38] Héctor Bombín and Miguel A Martin-Delgado. Optimal resources for topological two-dimensional stabilizer codes: Comparative study. *Physical Review A*, 76(1):012305, 2007.
- [39] Nicholas Connolly, Vivien Londe, Anthony Leverrier, and Nicolas Delfosse. Fast erasure decoder for a class of quantum ldpc codes. *arXiv preprint arXiv:2208.01002*, 2022.
- [40] Nicolas Delfosse, Vivien Londe, and Michael E Beverland. Toward a union-find decoder for quantum ldpc codes. *IEEE Transactions on Information Theory*, 68(5):3187–3199, 2022.
- [41] Martin Hayhurst Appel, Alexey Tiranov, Simon Pabst, Ming Lai Chan, Christian Starup, Ying Wang, Leonardo Midolo, Konstantin Tiurev, Sven Scholz, Andreas D Wieck, et al. Entangling a hole spin with a time-bin photon: a waveguide approach for quantum dot sources of multiphoton entanglement. *Physical Review Letters*, 128(23):233602, 2022.
- [42] SE Thomas, M Billard, N Coste, SC Wein, H Ollivier, O Krebs, L Tazaïrt, A Harouri, A Lemaitre, I Sagnes, et al. Bright polarized single-photon source based on a linear dipole. *Physical review letters*, 126(23):233601, 2021.
- [43] Natasha Tamm, Alisa Javadi, Nadia Olympia Antoniadis, Daniel Najer, Matthias Christian Löbl, Alexander Rolf Korsch, Rüdiger Schott, Sascha René Valentin, Andreas Dirk Wieck, Arne Ludwig, et al. A bright and fast source of coherent single photons. *Nature Nanotechnology*, 16(4):399–403, 2021.
- [44] Ravitej Uppu, Freja T Pedersen, Ying Wang, Cecile T Olesen, Camille Papon, Xiaoyan Zhou, Leonardo Midolo, Sven Scholz, Andreas D Wieck, Arne Ludwig, et al. Scalable integrated single-photon source. *Science advances*, 6(50):eabc8268, 2020.
- [45] Mihir K Bhaskar, Ralf Riedinger, Bartholomeus Machielse, David S Levonian, Christian T Nguyen, Erik N Knall, Hongkun Park, Dirk Englund, Marko Lončar, Denis D Sukachev, et al. Experimental demonstration of memory-enhanced quantum communication. *Nature*, 580(7801):60–64, 2020.
- [46] Francesco Lenzini, Ben Haylock, Juan C Loredó, Raphael A Abrahao, Nor A Zakaria, Sachin Kasture, Isabelle Sagnes, Aristide Lemaitre, Hoang-Phuong Phan, Dzong Viet Dao, et al. Active demultiplexing of single photons from a solid-state source. *Laser & Photonics Reviews*, 11(3):1600297, 2017.
- [47] Mathias Pont, Riccardo Albiero, Sarah E Thomas, Nicolò Spagnolo, Francesco Ceccarelli, Giacomo Corrielli, Alexandre Briesset, Niccolò Somaschi, Héliot Huet, Abdelmounaim Harouri, et al. Quantifying n-photon indistinguishability with a cyclic integrated interferometer. *Physical Review X*, 12(3):031033, 2022.
- [48] Lena M Hansen, Lorenzo Carosini, Lennart Jehle, Francesco Giorgino, Romane Houvenaghel, Michal Vyvlecka, Juan C Loredó, and Philip Walther. Single-active-element demultiplexed multi-photon source. *arXiv preprint arXiv:2304.12956*, 2023.
- [49] Jonathan E Moussa. Transversal clifford gates on folded surface codes. *Physical Review A*, 94(4):042316, 2016.
- [50] Earl T Campbell. A theory of single-shot error correction for adversarial noise. *Quantum Science and Technology*, 4(2):025006, 2019.
- [51] Daniel Litinski and Naomi Nickerson. Active volume: An architecture for efficient fault-tolerant quantum computers with limited non-local connections. *arXiv preprint arXiv:2211.15465*, 2022.
- [52] Adam Paetznick and Krysta M Svore. Repeat-until-success: Non-deterministic decomposition of single-qubit unitaries. *arXiv preprint arXiv:1311.1074*, 2013.
- [53] Kerem Halil Shah and Daniel Kuan Li Oi. Ancilla driven quantum computation with arbitrary entangling strength. *arXiv preprint arXiv:1303.2066*, 2013.
- [54] Yuan Liang Lim, Sean D Barrett, Almut Beige, Pieter Kok, and Leong Chuan Kwek. Repeat-until-success quantum computing using stationary and flying qubits. *Physical Review A*, 73(1):012304, 2006.
- [55] Robert Raussendorf, Jim Harrington, and Kovid Goyal. Topological fault-tolerance in cluster state quantum computation. *New Journal of Physics*, 9(6):199, 2007.
- [56] Ying Li, Sean D Barrett, Thomas M Stace, and Simon C Benjamin. Fault tolerant quantum computation with nondeterministic gates. *Physical review letters*, 105(25): 250502, 2010.
- [57] Thomas J Bell, Jacob FF Bulmer, Alex E Jones, Stefano Paesani, Dara PS McCutcheon, and Anthony Laing. Protocol for generation of high-dimensional entanglement from an array of non-interacting photon emitters. *New Journal of Physics*, 24(1):013032, 2022.
- [58] JP Lee, B Villa, AJ Bennett, RM Stevenson, DJP Ellis, I Farrer, DA Ritchie, and AJ Shields. A quantum dot as a source of time-bin entangled multi-photon states. *Quantum Science and Technology*, 4(2):025011, 2019.
- [59] Arian Vezvaei, Paul Hilaire, Matthew F Doty, and Sophia E Economou. Deterministic generation of entangled photonic cluster states from quantum dot molecules. *Physical Review Applied*, 18(6):L061003, 2022.
- [60] Konstantin Tiurev, Martin Hayhurst Appel, Pol Llopart Mirambell, Mikkel Bloch Lauritzen, Alexey Tiranov, Peter Lodahl, and Anders Søndberg Sørensen. High-fidelity multiphoton-entangled cluster state with solid-state quantum emitters in photonic nanostructures. *Physical Review A*, 105(3):L030601, 2022.
- [61] Rui Vasconcelos, Sarah Reisenbauer, Cameron Salter,

- Georg Wachter, Daniel Wirtitsch, Jörg Schmiedmayer, Philip Walther, and Michael Trupke. Scalable spin-photon entanglement by time-to-polarization conversion. *npj Quantum Information*, 6(1):9, 2020.
- [62] Jean-Claude Besse, Kevin Reuer, Michele C Colloido, Arne Wulff, Lucien Wernli, Adrian Copetudo, Daniel Malz, Paul Magnard, Abdulkadir Akin, Mihai Gabureac, et al. Realizing a deterministic source of multipartite-entangled photonic qubits. *Nature communications*, 11(1):4877, 2020.
- [63] Chenxu Liu, Edwin Barnes, and Sophia Economou. Proposal for generating complex microwave graph states using superconducting circuits. In *Quantum 2.0*, pages QTu2A–21. Optica Publishing Group, 2022.
- [64] Yong Siah Teo, Hyunseok Jeong, Jaroslav Řeháček, Zdeněk Hradil, Luis L Sánchez-Soto, and Christine Silberhorn. On the prospects of multiport devices for photon-number-resolving detection. *Quantum Reports*, 1(2):162–180, 2019.
- [65] Note2. In principle, for perfectly indistinguishable photons, it is impossible to obtain a (0,1) or a (2,3) detection outcome. However, this is possible for distinguishable sources, and they correspond to an identity gate (up to a $Z_a Z_b$ outcome for the (2,3) detection).
- [66] Craig Gidney. Stim: a fast stabilizer circuit simulator. *Quantum*, 5:497, 2021.
- [67] Oscar Higgott. Pymatching: A python package for decoding quantum codes with minimum-weight perfect matching. *ACM Transactions on Quantum Computing*, 3(3):1–16, 2022.
- [68] Oscar Higgott and Craig Gidney. Sparse blossom: correcting a million errors per core second with minimum-weight matching. *arXiv preprint arXiv:2303.15933*, 2023.
- [69] Thomas M Stace and Sean D Barrett. Error correction and degeneracy in surface codes suffering loss. *Physical Review A*, 81(2):022317, 2010.
- [70] Stefano Paesani and Benjamin J Brown. High-threshold quantum computing by fusing one-dimensional cluster states. *arXiv preprint arXiv:2212.06775*, 2022.
- [71] Paul Hilaire, Yaron Castor, Edwin Barnes, Sophia E Economou, and Frédéric Grosshans. Linear optical logical bell state measurements with optimal loss-tolerance threshold. *arXiv preprint arXiv:2302.07908*, 2023.
- [72] Joschka Roffe, David R White, Simon Burton, and Earl Campbell. Decoding across the quantum low-density parity-check code landscape. *Physical Review Research*, 2(4):043423, 2020.
- [73] Jean-Pierre Tillich and Gilles Zémor. Quantum ldpc codes with positive rate and minimum distance proportional to the square root of the blocklength. *IEEE Transactions on Information Theory*, 60(2):1193–1202, 2013.
- [74] Sergey Bravyi, Andrew W Cross, Jay M Gambetta, Dmitri Maslov, Patrick Rall, and Theodore J Yoder. High-threshold and low-overhead fault-tolerant quantum memory. *arXiv preprint arXiv:2308.07915*, 2023.
- [75] Nikolas P Breuckmann and Vivien Londe. Single-shot decoding of linear rate ldpc quantum codes with high performance. *IEEE Transactions on Information Theory*, 68(1):272–286, 2021.
- [76] Qian Xu, Alireza Seif, Haoxiong Yan, Nam Mannucci, Bernard Ousmane Sane, Rodney Van Meter, Andrew N Cleland, and Liang Jiang. Distributed quantum error correction for chip-level catastrophic errors. *Physical review letters*, 129(24):240502, 2022.
- [77] James Ang, Gabriella Carini, Yanzhu Chen, Isaac Chuang, Michael Austin DeMarco, Sophia E Economou, Alec Eickbusch, Andrei Faraon, Kai-Mei Fu, Steven M Girvin, et al. Architectures for multinode superconducting quantum computers. *arXiv preprint arXiv:2212.06167*, 2022.
- [78] Matthias C Löbl, Stefano Paesani, and Anders S Sørensen. Loss-tolerant architecture for quantum computing with quantum emitters. *arXiv preprint arXiv:2304.03796*, 2023.
- [79] Srikrishna Omkar, Seok-Hyung Lee, Yong Siah Teo, Seung-Woo Lee, and Hyunseok Jeong. All-photonic architecture for scalable quantum computing with greenberger-horne-zeilinger states. *PRX Quantum*, 3(3):030309, 2022.
- [80] Brendan Pankovich, Angus Kan, Kwok Ho Wan, Maike Ostmann, Alex Neville, Srikrishna Omkar, Adel Sohbi, and Kamil Brádler. High photon-loss threshold quantum computing using ghz-state measurements. *arXiv preprint arXiv:2308.04192*, 2023.
- [81] Bikun Li, Sophia E Economou, and Edwin Barnes. Photonic resource state generation from a minimal number of quantum emitters. *npj Quantum Information*, 8(1):11, 2022.
- [82] Nicolas Maring, Andreas Fyrrillas, Mathias Pont, Edouard Ivanov, Petr Stepanov, Nico Margaria, William Hease, Anton Pishchagin, Thi Huong Au, Sébastien Boissier, et al. A general-purpose single-photon-based quantum computing platform. *arXiv preprint arXiv:2306.00874*, 2023.
- [83] Mete Atatüre, Dirk Englund, Nick Vamivakas, Sang-Yun Lee, and Joerg Wrachtrup. Material platforms for spin-based photonic quantum technologies. *Nature Reviews Materials*, 3(5):38–51, 2018.
- [84] Matthias Bock, Pascal Eich, Stephan Kucera, Matthias Kreis, Andreas Lenhard, Christoph Becher, and Jürgen Eschner. High-fidelity entanglement between a trapped ion and a telecom photon via quantum frequency conversion. *Nature communications*, 9(1):1998, 2018.
- [85] Anna Tchebotareva, Sophie LN Hermans, Peter C Humphreys, Dirk Voigt, Peter J Harmsma, Lun K Cheng, Ad L Verlaan, Niels Dijkhuizen, Wim De Jong, Anaïs Dréau, et al. Entanglement between a diamond spin qubit and a photonic time-bin qubit at telecom wavelength. *Physical review letters*, 123(6):063601, 2019.
- [86] P Siyushev, K Xia, R Reuter, M Jamali, N Zhao, N Yang, C Duan, N Kukharchyk, AD Wieck, R Kolesov, et al. Coherent properties of single rare-earth spin qubits. *Nature communications*, 5(1):3895, 2014.
- [87] Andrei Ruskuc, Chun-Ju Wu, Jake Rochman, Joonhee Choi, and Andrei Faraon. Nuclear spin-wave quantum register for a solid-state qubit. *Nature*, 602(7897):408–413, 2022.
- [88] Daniel B Higginbottom, Alexander TK Kurkjian, Camille Chartrand, Moein Kazemi, Nicholas A Brunelle, Evan R MacQuarrie, James R Klein, Nicholas R Lee-Hone, Jakub Stacho, Myles Ruether, et al. Optical observation of single spins in silicon. *Nature*, 607(7918):266–270, 2022.

- [89] Chang-Min Lee, Fariba Islam, Samuel Harper, Mustafa Atabey Buyukkaya, Daniel Higginbottom, Stephanie Simmons, and Edo Waks. High-efficiency single photon emission from a silicon t-center in a nanobeam. *arXiv preprint arXiv:2308.04541*, 2023.
- [90] Stefania Castelletto, Faraz A Inam, Shin-ichiro Sato, and Alberto Boretti. Hexagonal boron nitride: a review of the emerging material platform for single-photon sources and the spin-photon interface. *Beilstein Journal of Nanotechnology*, 11(1):740–769, 2020.
- [91] Alexander Kubanek. Coherent quantum emitters in hexagonal boron nitride. *Advanced Quantum Technologies*, 5(9):2200009, 2022.
- [92] Raj N Patel, Rebecca EK Fishman, Tzu-Yung Huang, Jordan A Gusdorff, David A Fehr, David A Hopper, S Alex Breitweiser, Benjamin Porat, Michael E Flatté, and Lee C Bassett. Dynamical characterization and room-temperature control of an optically addressable single spin in hexagonal boron nitride. *arXiv preprint arXiv:2309.05604*, 2023.
- [93] James M Auger, Hussain Anwar, Mercedes Gimeno-Segovia, Thomas M Stace, and Dan E Browne. Fault-tolerant quantum computation with nondeterministic entangling gates. *Physical Review A*, 97(3):030301, 2018.
- [94] Tom J Bell, Love A Pettersson, and Stefano Paesani. Optimising graph codes for measurement-based loss tolerance. *arXiv preprint arXiv:2212.04834*, 2022.
- [95] Hector Bombín, Chris Dawson, Naomi Nickerson, Mihir Pant, and Jordan Sullivan. Increasing error tolerance in quantum computers with dynamic bias arrangement. *arXiv preprint arXiv:2303.16122*, 2023.
- [96] Daniel Gottesman. Fault-tolerant quantum computation with constant overhead. *arXiv preprint arXiv:1310.2984*, 2013.
- [97] Omar Fawzi, Antoine Gropellier, and Anthony Leverrier. Constant overhead quantum fault tolerance with quantum expander codes. *Communications of the ACM*, 64(1):106–114, 2020.
- [98] Lawrence Z Cohen, Isaac H Kim, Stephen D Bartlett, and Benjamin J Brown. Low-overhead fault-tolerant quantum computing using long-range connectivity. *Science Advances*, 8(20):eabn1717, 2022.
- [99] Heinz-Peter Breuer and Francesco Petruccione. *The theory of open quantum systems*. Oxford University Press, USA, 2002.
- [100] Chong-Ki Hong, Zhe-Yu Ou, and Leonard Mandel. Measurement of subpicosecond time intervals between two photons by interference. *Physical review letters*, 59(18):2044, 1987.
- [101] Matt McEwen, Dave Bacon, and Craig Gidney. Relaxing hardware requirements for surface code circuits using time-dynamics. *arXiv preprint arXiv:2302.02192*, 2023.
- [102] Note3. This solution was provided by Craig Gidney in <https://quantumcomputing.stackexchange.com/questions/26582/how-do-i-perform-an-erasure-error-in-stim>.
- [103] Martin Suchara, Andrew W. Cross, and Jay M. Gambetta. Leakage suppression in the toric code. In *2015 IEEE International Symposium on Information Theory (ISIT)*, pages 1119–1123, 2015. doi: 10.1109/ISIT.2015.7282629.